# Highly Sensitive in-Plane Strain Mapping

# Using a Laser Scanning Technique

by

Hanshuang Liang

A Dissertation Presented in Partial Fulfillment
of the Requirements for the Degree
Doctor of Philosophy

Approved November 2014 by the
Graduate Supervisory Committee:

Hongbin Yu, Chair
Poh Chieh Benny Poon
Hanqing Jiang
Yong-Hang Zhang

ARIZONA STATE UNIVERSITY

December 2014

# ABSTRACT

In this work, a highly sensitive strain sensing technique is developed to realize in-plane strain mapping for microelectronic packages or emerging flexible or foldable devices, where mechanical or thermal strain is a major concern that could affect the performance of the working devices or even lead to the failure of the devices. Therefore strain sensing techniques to create a contour of the strain distribution is desired.

The developed highly sensitive micro-strain sensing technique differs from the existing strain mapping techniques, such as digital image correlation (DIC)/micro-Moiré techniques, in terms of working mechanism, by filling a technology gap that requires high spatial resolution while simultaneously maintaining a large field-of-view. The strain sensing mechanism relies on the scanning of a tightly focused laser beam onto the grating that is on the sample surface to detect the change in the diffracted beam angle as a result of the strain. Gratings are fabricated on the target substrates to serve as strain sensors, which carries the strain information in the form of variations in the grating period. The geometric structure of the optical system inherently ensures the high sensitivity for the strain sensing, where the nanoscale change of the grating period is amplified by almost six orders into a diffraction peak shift on the order of several hundred micrometers. It significantly amplifies the small signal measurements so that the desired sensitivity and accuracy can be achieved.

The important features, such as strain sensitivity and spatial resolution, for the strain sensing technique are investigated to evaluate the technique. The strain sensitivity has been validated by measurements on homogenous materials with well known reference values of CTE (coefficient of thermal expansion). 10 micro-strain has been

successfully resolved from the silicon CTE extraction measurements. Furthermore, the spatial resolution has been studied on predefined grating patterns, which are assembled to mimic the uneven strain distribution across the sample surface. A resolvable feature size of 10 μm has been achieved with an incident laser spot size of 50 μm in diameter.

In addition, the strain sensing technique has been applied to a composite sample made of SU8 and silicon, as well as the microelectronic packages for thermal strain mappings.

ACKNOWLEDGMENTS

I would like to express my deepest appreciation to committee chair, Prof. Hongbin Yu, who has the attitude and the substance of a genius: he continually convincingly conveyed a spirit of adventure in regard to research and scholarship, and an excitement in regard to teaching. Without his guidance and persistent help, this dissertation would not have been possible.

I would like to express my sincere appreciations to Prof. Hanqing Jiang, Dr. Benny Poon and Dr. Min Tao for their great guidance and support for Intel SRS project for the past three years. This great collaboration experience inspired me tremendously through all those discussions, monthly and annual review meetings, etc.

I would like to thank Prof. Liping Wang and Prof. Yong-Hang Zhang for making time to serve on my committee and broadening my knowledge by their questions and comments.

I would like to thank my colleagues in Prof. Hongbin Yu's group: Dr. Hao Wu, Ebraheem Azhar, Seungho Ahn, Jhih-Hong Peng, George Chen, Hoa Nguyen, Michael Saxon, Todd Houghton.

I would like to thank my other collaborators: Dr. Teng Ma, Dr. Rui Tang, Dr. Hai Huang, Zeming Song, Cheng Lv, Xu Wang, Yiling Fan, Mengbing Liang.

TABLE OF CONTENTS

Page

CHAPTER Page

LIST OF TABLES

LIST OF FIGURES

Figure Page

Figure Page

Figure Page

Figure Page

Figure Page

# CHAPTER 1

## Introduction

Strain distribution exists among all mechanical and electronic devices, including the emerging flexible[1-10] and foldable devices[11-16], when subject to mechanical bending or elevated temperature. In most cases, it affects the mechanical and electrical properties of the devices and lead to the failure of the devices. For example, microelectronic packages[17-19] are getting smaller and smaller on demand of the market. This aggravates the integration of different materials within the package and brings about more heat dissipation. When the electronic package is working with increased temperature, the layers of different materials will expand to different degrees due to coefficient of thermal expansion (CTE) mismatch coming from the materials. Consequently, the deformations among those layers brings in the strain unevenly across the whole package. The spots experiencing the highest strain are most likely to be the failure points for the electronic packages. Thus an accurate strain mapping technique is of great interest and could provide detailed understanding of the strain distribution across devices, thus helping to improve the structure or layout design of the mechanical and electronic devices.

## 1.1 Potential Market

There are many areas in mechanical testing that need high spatial resolution, high sensitivity and large field-of-view strain mapping, such as structural testing that requires full-field mapping with high spatial details; and more recently increasing interest in electronics packaging applications where stress from integrating different materials in increasingly smaller packages becomes a major failure point in the industry, which requires understanding and control. Research institutions, university labs, components and packaging companies and most semiconductor companies, such as Intel Corp., are all primary candidates who will be interested in acquiring such tools for their research, development and product quality monitoring.

In order to get an overview of the strain sensing needs in the market and in academia, a preliminary survey to count the numbers of published papers related to strain measurement per year on two leading publications in the area is conducted, presented in Table 1. The publications are Electronic Component Technology Conference (ECTC) where major microelectronics packaging related research and development work are published, and the journal of Experimental Mechanics where many studies using strain mapping are reported, mainly from academia.

Table 1. Summary of ECTC 2010-2012 and Experimental Mechanics 2011-2012

| | ECTC | | | Exp. Mech. | |
|---|---|---|---|---|---|
| **# of papers/year** | 2010 | 2011 | 2012 | 2011 | 2012 |
| **Moiré** | 15 | 13 | 18 | 2 | 2 |
| **DIC** | 6 | 4 | 4 | 20 | 30 |
| **Others** | 3 | 5 | 3 | 5 | 7 |

From the ECTC survey between 2010 -2012, 37 leading semiconductor companies were in the market for high spatial resolution, high sensitivity strain mapping tools, such as Intel Corp., IBM Corp., Taiwan Semiconductor Manufacturing Company, Ltd. (Taiwan) (TSMC), Fujitsu, Advanced Micro Devices, Inc. (AMD), Samsung Electronics Co., Cisco Systems, Micron Technologies, Broadcom Corp., Hitachi, Texas Instruments, Infineon Technologies, QUALCOMM Inc., and Fraunhofer Institute IZM. Interestingly, there are more users from industrial companies than academia, likely due to 1) the higher initial cost of ownership, and 2) more significantly, the need to attach high resolution gratings to the sample surface, which is typically not easy to realize and expensive. As illustrated in this work, our buckled thin film grating and direct grating fabrication technique would greatly reduce the difficulty in 2).

On the other hand, from a survey of the journal Experimental Mechanics within less than two years between 2011-2012, there were 59 universities and research institutes that

have used strain mapping tools, primarily digital image correlations (DICs), in a wide range of research topics, including microstructure mechanics, residual stress analysis, micro-fracture analysis, composite materials, biomechanics. Compared to Moiré analysis tool, optical DIC tools are relatively low cost for university to own. For instance, in the ASU Mechanical Engineering Department alone, there are at least four DIC tools routinely being used for mechanics analysis.

The survey reveals a big need for strain sensing technique development in the market. It depicts a great outlook if our prototype can be proved to offer what DIC and Moiré can not.

## 1.2 Contemporary Strain Sensing Techniques

Traditional in-plane mechanical strain is measured using a strain gauge or an optical fiber strain gauge. Typically, these strain sensors are large in size, and they are designed mainly for single point strain measurement on large surfaces. They are not capable of mapping out strain at finer scale. Instead, to perform spatial mapping of strain, several non-contact measurement techniques have been used extensively, driven in large part by the electronics packaging community, where high spatial resolution of strain distribution among different chip and packaging materials are desired. Among these techniques are micro Moiré[20-25], optical digital image correlation (DIC)[24, 26-30] and scanning electron microscope (SEM) DIC[22, 31-34].

Micro Moiré: The Moiré technique is featured for its full-field measurement capability. Moiré patterns are formed by a pair of coherent light from two superimposed grating which have slight variations, such as differences in tilted angles or grating periods[23]. Fringe sensitivity is determined[24] by d = 1/(2f), where d is the change in displacement between successive fringes. For f = 1200 lines/mm, d is 0.417 μm. Higher sensitivity can be achieved by applying a denser grating[25]. Due to the diffraction limit, the light source wavelength has to be smaller than the grating wavelength. For example, a specimen fabricated with a 5000 lines/mm grating can be tested by a SEM Moiré using an electron beam with a certain line scan rate[21]. By introducing the phase-shifting technique[35-41], the in-plane displacement resolution can be further improved. However, the strain information is not localized. Instead, the strain of the Moiré pattern is determined by the field of view. Hence, this metrology is largely limited by the spatial resolution. It cannot have more than ½ the displacement resolution in one pixel for fringes to be noticeable. Performing a Moiré measurement can be complicated and time consuming. As curved lines or lines that are not exactly parallel add to the complexity of the Moiré pattern, it is crucial to have a high quality grating attached to the target sample. In addition, a flat surface on the specimen is necessary for the technique in most cases. Therefore, it has limited applications in strain measurements on 3D-surfaces.

DIC and SEM DIC: DIC is a very popular technique for stain mapping in engineering mechanics. Compared to Moiré, no special surface preparation is

required[26]. Hence, it is more flexible in the choice of a specimen's geometry[42]. DIC techniques can achieve high spatial resolution with high in-plane displacement resolution. However, this compromises the field of view, as a large optical magnification is required, and becomes a limiting factor when detailed strain mapping in a large area is needed. The spatial resolution and sensitivity of DIC is strongly reliant on the imaging system. The development and advancement of imaging systems have broadened the applications of DIC methods, such as DIC coupled with an optical microscope[39, 43-46], DIC coupled with SEM[47-55], DIC coupled with atomic force microscope[56-60]. The highest spatial resolution of strain mapping can be achieved using SEM DIC. The instrument, which is housed in a vacuum system, however, has a much higher cost and a very limited field of view for many practical applications.

## 1.3 The Developed Micro-Strain Sensing Technique

We developed a highly sensitive micro-strain sensing technique that is different from the existing strain mapping techniques, in terms of working mechanism, filling a technology gap between micro Moiré/optical DIC and SEM DIC, that requires a high spatial resolution while simultaneously offering a large field-of-view[61].

In this approach, the laser spot size determines the maximum feature size for strain to be measured accurately. The strain measured is localized and decoupled from the field of view. For a laser spot size of 200 μm, an in-plane displacement resolution of 2.5 nm is

obtained. An expectation of 0.25 nm resolution is achievable when the laser spot size is reduced down to 5 μm. A large field of view can be realized by incorporating an advanced motorized stage with a long travel distance and small stepping size. Table 2 summaries the key figures of merit of the in-plane strain sensing techniques.

Table 2. Comparison of Several in-Plane Strain Measurement Techniques

| | Micro Moiré | Optical DIC | SEM DIC | **This Strain Sensor** |
|---|---|---|---|---|
| In-plane displacement resolution | 52 nm | 3 μm | < 5 nm | 2.5 nm (measured) 0.25 nm (estimated) |
| Spatial resolution | 1.5 μm | 2 μm | 20 nm | < 1 μm (estimated) |
| Field of view | 1mm×1mm | < 1 mm×1 mm for high spatial resolution | < 50 μm×50 μm | > 1 cm×1 cm (determined by translation stage) |

CHAPTER 2

Working Principle

## 2.1 Strain Sensing Mechanism

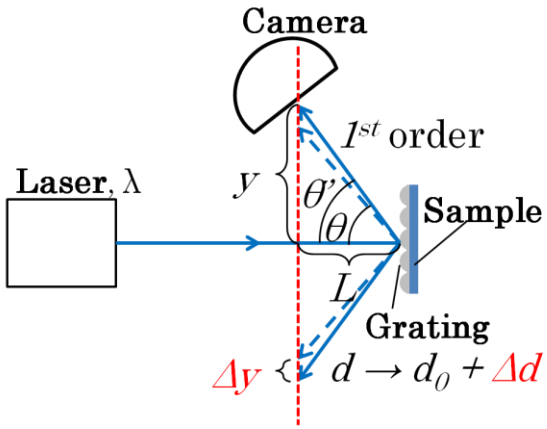


Figure 1. Schematic of the Strain Sensing Mechanism.

This mechanism starts from the simple diffraction equation,

$$d_0 \sin\theta = m\lambda \quad (1)$$

which relates the diffraction angle $\theta$, initial grating period $d_0$, laser source wavelength $\lambda$, and m is the order of diffraction when the laser beam is normal to the grating surface. As shown in the inset of Fig. 1, the optical setup for strain measurement, a geometric relation,

$$\tan\theta = \frac{y}{L} \quad (2)$$

relates the horizontal position $L$ of the specimen and vertical position $y$ of the photo detector.

When a strain is induced on the specimen through either mechanical or thermal means, the grating period changes from $d_0$ to $d$ (= $d_0$ + $\Delta d$) and leads to the change in

diffraction angle $\theta$ by $\Delta\theta$. Meanwhile, the change of $\theta$ results in the change of $y$ by $\Delta y$, which is linearly dependent on $\Delta d$, as shown below,

$$\Delta y = -C\Delta d \tag{3}$$

where

$$C = \frac{\lambda L}{d_0^{\,2}\left(1-\frac{m^2\lambda^2}{d_0^2}\right)^{3/2}} \tag{4}$$

is a constant. It indicates a linear relationship between the diffraction peak displacement on the camera and the grating period variation on the sample surface. Strain is defined as

$$\varepsilon = \frac{\Delta d}{d_0} \tag{5}$$

This pre-factor $C$ actually functions as an amplification factor; a very small quantity $\Delta d$, typically in the nanometer range, is amplified to a microscopic and measurable quantity $\Delta y$ on the order of tens of microns. For example, giving $d_0$ = 833.33 nm (or equivalently, a grating density of 1200 lines/mm), $L$ = 10 cm and $\lambda$ = 632.8 nm (He-Ne laser wavelength), one obtains that this amplification factor $C$ is approximately $3.3\times10^5$. The primary reason for achieving such a large amplification is the large $L/d_0$ ratio, i.e., the detector is positioned far away from the sample, a similar mechanism that is employed in detecting nanometer scale cantilever bending in atomic force microscopy (AFM). This amplification factor $C$, can be further maximized by choosing a $d_0$ value that very close to $\lambda$, as shown in Table 3. For example, if one chooses $\lambda$ = 633 nm, $d_0$ = 700 nm, and the amplification factor $C$ (= 1,660,138) from Table 1, a variation of buckling periodicity $\Delta d$ of 0.07 nm causes $\Delta y$ value of 116 μm, which is the shift of the 1st order diffraction peak position at the detector that can be easily reached by the stages in the optical setup. This example indicates a very small strain $\Delta d/d_0$ of 0.01% can be amplified

into a large angle and thus position difference at the optical detector. In this way, the strain information carried by the variation of the grating periodicity is amplified by orders of magnitudes when the initial values are properly chosen, which forms the mechanism of strain sensing using buckled stiff thin films on soft substrates.

Table 3. Calculated Values of Amplification Factor $C$ for Different $\lambda$ and $d_0$ Combinations. Assume $L$ = 10 cm

| $\lambda$ (nm) | $d_0$ (nm) | | | | |
|---|---|---|---|---|---|
| | 900 | 800 | 700 | 600 | 500 |
| 408 | 71,128 | 100,166 | 155,193 | 287,520 | 844,927 |
| 532 | 125,160 | 199,546 | 395,484 | 1,494,617 | N/A |
| 633 | 217,553 | 432,563 | 1,660,138 | N/A | N/A |

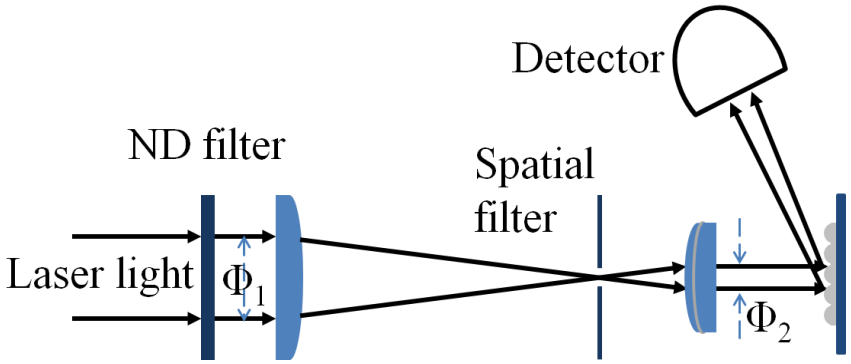


Figure 2. Design of the Optical Setup.

The optical testing system is then designed for the micro-strain sensing, as shown in Fig. 2. The light source is a 633 nm He-Ne laser with output power of 21 mW. The laser spot size is reduced from 700 μm ($\Phi_1$) to 200 μm ($\Phi_2$) in diameter at the grating surface through a pair of lenses. Further reduction can be realized by incorporation of an objective lens. The photo detector captures the profile of the first order diffraction signal, for the extraction of the diffraction signal peak position.

## 2.2 Diffraction Peak Shifting Simulation

Although the proposed method for strain measurement seems simple (Fig. 1), it is important to consider whether or not the shift in the peak position of the diffraction light due to a small strain can be differentiated. The laser spot size is an important parameter to consider. Fig. 3 shows the simulation model with a *N*-slit grating, where *N* is the number of slits with periodicity *d* (= *a* + *b*) for each slit. In other words, it is assumed that the laser light is shone on these *N* slits with a spot size of *Nd*. Within each slit, the opening and blocking region sizes are defined as *a* and *b*, respectively. The detector is modeled as a screen. It is assumed that plane wave is incident and normal to the slits with a fixed ratio of *d/a*. The superposition of the waves from all the points within a single slit at point *P*, on the screen has an expression of,

$$U_1 = \int du_1 \int_0^a \frac{A_0}{a} e^{-i\omega t} e^{ikx\sin\theta} dx \qquad (6)$$

where $A_0$ is the amplitude of the waves, $k = 2\pi/\lambda$ is the wave number of the incident light. The integration is over the opening area of the single slit.

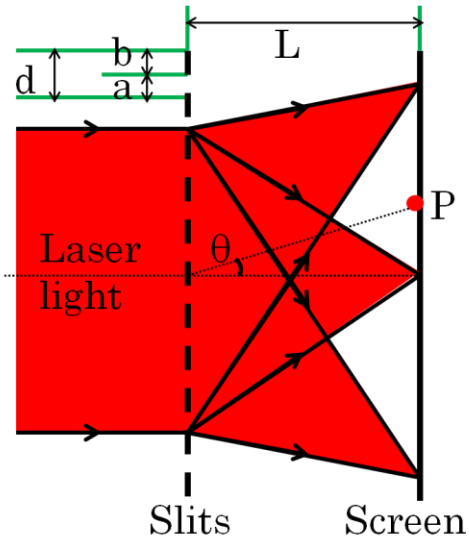


Figure 3. Simulation Model for Diffraction Peak Shift.

At point *P*, the contribution from all *N* slits is expressed as the summation over all these *N* slits,

$$U = A_0 \frac{\sin\alpha}{\alpha} \frac{\sin N\beta}{\beta} \exp\left\{ i \frac{\left[a + (N-1)\right]\sin\theta}{\lambda} \omega t \right\} \tag{7}$$

where $\alpha = (\pi a/\lambda)\sin\theta$, $\beta = (\pi d/\lambda)\sin\theta$.

Thus, the light intensity profile at point *P* is given by

$$I_P = U^2 = I_0 \left( \frac{\sin\alpha}{\alpha} \right)^2 \left( \frac{\sin N\beta}{\beta} \right)^2 \tag{8}$$

where $I_0 = A_0^2$ is the intensity of light impinging on the diffraction grating.

The following MATLAB code is written to calculate the diffraction light distribution on the screen, according to Eq. (8).

MATLAB code:

```
%N slit diffraction
clear
lamda=633e-9;% laser source wavelength
a=3e-7;d=2*a;L=0.1;N=16;
% L is the distance between grating and detector
% illuminated width of grating: a
% d is the spacing between slits
% N is the number of slits
xm=0.2;%xm=2*lamda*L/a, xm defines display range on screen;
y0=xm;
alpha_in=0/180*pi % alpha_in is defined as the incident angle;
n=40001; % mesh
x0=linspace(-0.2,0.2,n);
for i=1:n
sinphi_int=sin(atan(x0(i)/L))-sin(alpha_in);
sinphi_diff=sin(atan(x0(i)/L));
alpha=pi*a*sinphi_diff/lamda;
beta=pi*d*sinphi_int/lamda;
B(i,:)=(sin(alpha)./alpha).^2.*(sin(N*beta)./sin(beta)).^2;
B1=B/max(B);
end
NC=255;
```

```
Br=(B/max(B))*NC;
subplot(1,2,1)
image(y0,x0,Br);
colormap(gray(NC));
subplot(1,2,2)
plot(B1,x0);
```

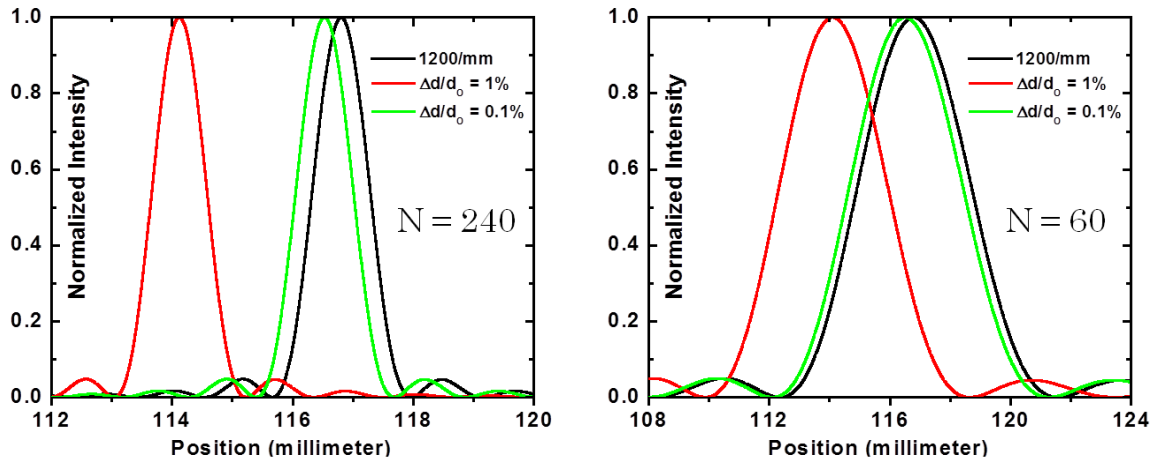


Figure 4. Diffracted Beam Intensity Simulations Based on the Multi-Slit Grating Model Shown in Fig. 3, with Grating to Screen Distance L = 10 cm. Small Variations are Applied to the Grating Periodicity to Obtain the Peak Shift, as Illustrated in (a) and (b). Spot Size is 200 μm (or Number of Slits N = 240) in (a), and 50 μm (or N = 60) in (b).

Figure 4(a) shows the first order diffraction patterns with a laser spot size of 200 μm and grating to screen distance $L$ = 10 cm. The black line indicates the measurement when no strain is applied, while the red and green lines represent intensity profile when 1% and

0.1% strain applied, respectively. In this case, the laser wavelength is set to be 633 nm, the number of slits N is set to be 240, and the initial grating period is 833.3 nm (i.e., 1,200 lines/mm). Fig. 4(b) shows the same results as Fig. 4(a) but with a 50 μm laser spot size. It is clear that a smaller grating period variation leads to a smaller peak shift. This comparison suggests that a detector with high sensitivity is required to capture the localized strain variation with a very small laser spot size. Quantitative analysis indicating further reducing laser spot size to 10 μm and with N = 12 for d = 800 nm grating, a 0.1% strain will lead to light intensity change on the order of $10^{-4}$, well within the limit of the auto-balanced photo detector chosen in the experiment. The strain sensitivity in our detection scheme can be estimated. The auto-balanced photodetector used in our experiment can detect optical intensity variation on the order of $10^{-6}$, therefore 1 nW intensity difference for 1 mW signal due to diffraction peak shift can be translated to a strain of $2.3 \times 10^{-6}$ for a laser spot size of 200 μm from simulation and through Eq. (3).

Eventually, the laser spot size will be reduced in order to improve the spatial resolution. However, the smaller laser spot size will result in fewer grating lines illuminated by the laser, which causes the diffraction signals to be weaker. In order to solve this problem, one can apply denser gratings[25] to the target substrates, as calculated in Table 4, when the incident laser wavelength is 633 nm. The incident laser spot size is assumed to be 10 μm. The comparison is between the calculation with no strain applied and with 0.1% strain applied to the simulated gratings. The calculated results reveal that denser gratings generate larger diffraction peak shifts as well as astronger diffraction s ignal intensity, which benefits the strain sensing testing

significantly. However, according to the grating equation, Eq. (1), d has to be larger than λ to make the equation valid. If we would like to apply gratings with period smaller than 633 nm, a shorter output wavelength laser must be applied as well. As calculated in Table 5, the incident laser wavelength is 405 nm.

Table 4. Simulation of the Diffraction Peak Shifts, when the Grating Period is varied, Given the Incident Laser Spot Size Remains 10 μm in Diameter. The Incident Laser Wavelength is 633 nm.

| D (nm) | N | Peak position (m) | Peak shift (μm) | Normalized intensity difference (%) | Required minimum resolution |
|---|---|---|---|---|---|
| 650 | 15 | 0.4177825 | 7,507.5 | 0.073792 | 1356 |
| 700 | 14 | 0.21002 | 1,120 | 0.063639 | 1572 |
| 750 | 13 | 0.15638125 | 537.5 | 0.055146 | 1814 |
| 800 | 12 | 0.128665 | 340 | 0.046377 | 2157 |

Table 5. Simulation of the Diffraction Peak Shifts, when the Grating Period is Varied, Given the Incident Laser Spot Size Remains 10 μm in Diameter. The Incident Laser Wavelength is 405 nm.

| D (nm) | N | Peak position (m) | Peak shift (μm) | Normalized intensity difference (%) | Required minimum resolution |
|---|---|---|---|---|---|
| 450 | 22 | 0.20579375 | 1,068.75 | 0.158752 | 630 |
| 500 | 20 | 0.13782 | 400 | 0.131802 | 759 |
| 550 | 18 | 0.1086125 | 237.5 | 0.106474 | 940 |
| 600 | 16 | 0.0912875 | 167.5 | 0.084963 | 1177 |
| 650 | 15 | 0.079485 | 130 | 0.073728 | 1357 |
| 700 | 14 | 0.07077 | 106.25 | 0.064372 | 1554 |
| 750 | 13 | 0.063995 | 90 | 0.054813 | 1825 |
| 800 | 12 | 0.058535 | 77 | 0.046603 | 2146 |

# CHAPTER 3

## Grating Samples

Several types of gratings have been utilized in the project, as listed in the following Table 6. We have reported a strain sensing approach that utilize PDMS wrinkling as an optical grating to measure thermally-induced strain of different homogenous materials[62]. This spontaneously generated wrinkle has been proposed for various applications including stretchable electronics[63-68], tunable gratings[69-75], lithium ion batteries[76] and submicron pattern production[77, 78] due to the ease of fabrication by integrating hard materials with soft substrates. Such PDMS buckling needs to be bonded to the target substrates for the strain sensing. It is easy to fabricate with low cost. And the fabricated grating period is controllable by choosing the proper initial conditions, which will be discussed later. However, bonding can be very challenging when apply to certain substrates, such as copper and glass. Furthermore, simulation work indicates the thickness of the grating prevents the accurate strain information to be sensed.

There are several methods to create zero-thickness gratings. Soft contact lithography[78-84] with the PDMS buckling utilized as a photo-mask is a low-cost solution. One can create a large grating if a large area strain mapping is required. However, the quality of the grating patterns are not ideal, in terms of the uniformity. It will add more complexity to the strain sensing. Electron beam lithography[85] (EBL) is another solution to create zero-thickness gratings with better uniformity than soft contact lithography. However, it is not applicable to write larger area grating patterns, since the EBL writing time is heavily dependent on the area of the pattern. Both the soft contact lithography and EBL require a step where photoresit is spin-coated onto the target

substrates, which may not be applicable for certain samples, such as for the cross-section of microelectronic packages. In this case, focused ion beam (FIB) is utilized to write grating patterns. FIB is a high cost solution and, similar to EBL, takes a long time for the pattern writing. Thus, it can only be applied to write grating patterns on a small region of interest.

Other possible solutions to fabricate zero-thickness gratings include deep ultraviolet (DUV) lithography[86, 87], interference lithography[88-90], nanoimprint lithography[91-93], self-assembly[94] and so on.

Table 6. Different Types of Gratings Utilized in the Strain Sensing Measurements.

| Grating thickness | Fabrication method | Notes |
|---|---|---|
| Finite thickness | PDMS buckling | Easy to fabricate but hard to bond. |
| Zero-thickness | Soft contact lithography | Applicable to flexible and smooth substrates. |
| | Electron beam lithography | Work on rigid and smooth substrates. |
| | Focus ion beam writing | No photolithography needed; any substrates. |

3.1 PDMS Gratings

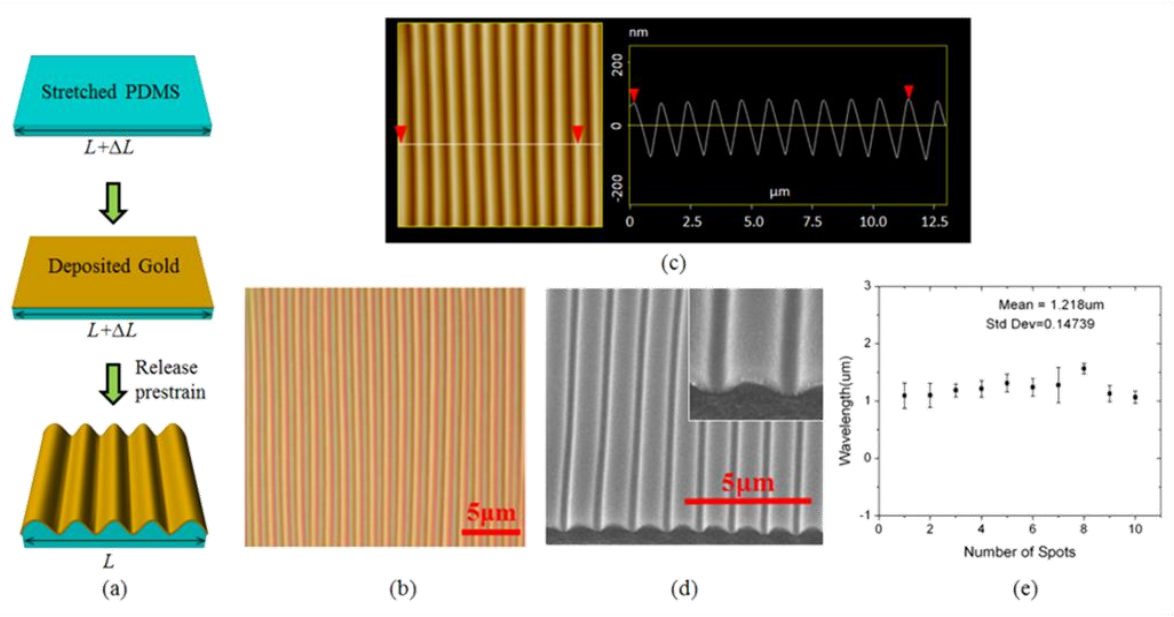


Figure 5. (a) Schematic of the Fabrication Process for PDMS/Au Grating. (b) Optical Microscopy Image and (c) AFM Image of Wrinkling Profile of PDMS/Au Grating Surface. (d) SEM image of Wrinkles. (e) Wrinkling Wavelength (Period) Distribution at Ten Different Spots over a Surface Area of 100 × 100 μm$^2$. The Wrinkling Period Remains Largely Constant over this Surface Area, in Good Agreement with the Calculated Period Value by Eq. (9). The Error Bars are One Standard Deviation of the Data, which is Taken as the Experimental Uncertainty of the Measurement.

Figure 5(a) illustrates the fabrication flow of the PDMS/Au tunable grating. A polydimethylsiloxane (PDMS) elastomer (Sylgard 184, Dow Corning) was made by mixing the base component and the curing agent in a 10:1 ratio by weight, followed by de-gassing and curing at 80°C for 3 hours. A slab of PDMS elastomer (0.1-1 mm thick) was mounted and elastically stretched on a home-made stage with designed uniaxial pre-

strain. After being exposed to oxygen plasma (50 W) for 1 minute to enhance the adhesion, the pre-strained PDMS slab was sputter-coated with a gold (90%)/palladium (10%) (Au/Pd) alloy film of nanoscale thickness. The addition of palladium to gold increases its bonding strength, known as white gold. Due to the small proportion of palladium we will refer to the alloy as gold. Finally, the relaxation of the pre-strain in the PDMS substrates compresses the Au thin film, leading to the deformation and wrinkling in both the Au film and PDMS substrate surface in a sinusoidal pattern. This is a result of the minimization of the system's potential energy by the out-of-plane deformation. The wrinkling period, *d*, is determined by the mechanical properties of Au film and PDMS substrate, the pre-strain $\varepsilon_{pre}$, and the thickness of the gold film[95], as described previously[69]

$$d = \frac{2\pi h_f}{\left(1+\varepsilon_{pre}\right)\left[1+\frac{5}{32}\varepsilon_{pre}\left(1+\varepsilon_{pre}\right)\right]^{1/3}}\left[\frac{E_f\left(1-\nu_s^2\right)}{3E_s\left(1-\nu_f^2\right)}\right]^{1/3} \qquad (9)$$

where $h_f$ is the thickness of the Au film, $E$ is Young's modulus and $\nu$ is Poisson's ratio. The subscripts "s" and "f" refer to the PDMS substrate and Au film, respectively. By varying the pre-strain $\varepsilon_{pre}$ and the Au film thickness $h_f$, the buckling period $d$ can be tuned with a broad range. In this work, the buckling period is in the order of micron or sub-micron range for the optimal grating efficiency for the visible light, which is employed for strain sensing application as discussed below.

Figure 5(b) shows an optical microscope image of a PDMS/Au grating fabricated by the above mentioned method, with $h_f$ = 10 nm, $\varepsilon_{pre}$ = 15%, and the measured buckling period $d$ = 1.22 μm, which agrees well with the calculated value of 1.20 μm obtained from Eq. (9) when the following material parameters are used, $E_f$ = 80 GPa, $E_s$ = 2 MPa,

$h_f$ = 10 nm, $v_f$ = 0.3, and $v_s$ = 0.4921. Fig. 5(c) shows the atomic force microscope (AFM) image of the grating topography and a line-scan profile, which illustrates the uniformity of the buckling in a small area. Fig. 5(d) illustrates scanning electron microscope (SEM) image of the continuous gold film along wave direction on PDMS. To examine the uniformity over a large area, the buckling periods were measured at ten different locations on an area of 100×100 $\mu m^2$ and the results are shown in Fig. 5(e). It was found that the buckling period is uniform over an area of tens of $\mu m^2$.

Using the alternative method of preparing the grating sample, PDMS grating is molded using a Thorlabs VIS reflective holographic grating with 1200 lines per millimeter, as shown in Fig. 6(b). The procedure is started by weighing PDMS prepolymer components in a 10:1 (prepolymer: curing agent) ratio in a plastic cup and then stirring for five minutes to create a homogeneous mixture. The plastic cup is then covered with aluminum foil to prevent contamination and left alone for 30 minutes until the bubbles dissipate. While the bubbles are being dissipated, 2-3 drops of perfluorooctyltrichlorosilane are added in a vacuum chamber for 30 minutes so that the PDMS will not adhere to the Petri dish or commercial grating. The Petri dish and commercial grating are removed after 30 minutes and the PDMS mixture is poured on top of the commercial grating until there is a thin uniform layer over the grating. The Petri-dish is then left out for another 30 minutes to allow all the bubbles to dissipate and then the Petri dish is put in an oven for two and a half hours at 85℃ to cure. After the PDMS has been cured, it is removed from the oven and carefully peeled from the commercial grating. Grating samples fabricated through this technique show better quality in terms of the uniformity of the buckled pattern in contrast to the first technique. However, the

periods of the grating samples prepared through this method are not tunable. The optical image confirms that there is good uniformity in the grating across the entire sample. The height of the grating is measured to be ~100 nm by atomic force microscope (AFM).

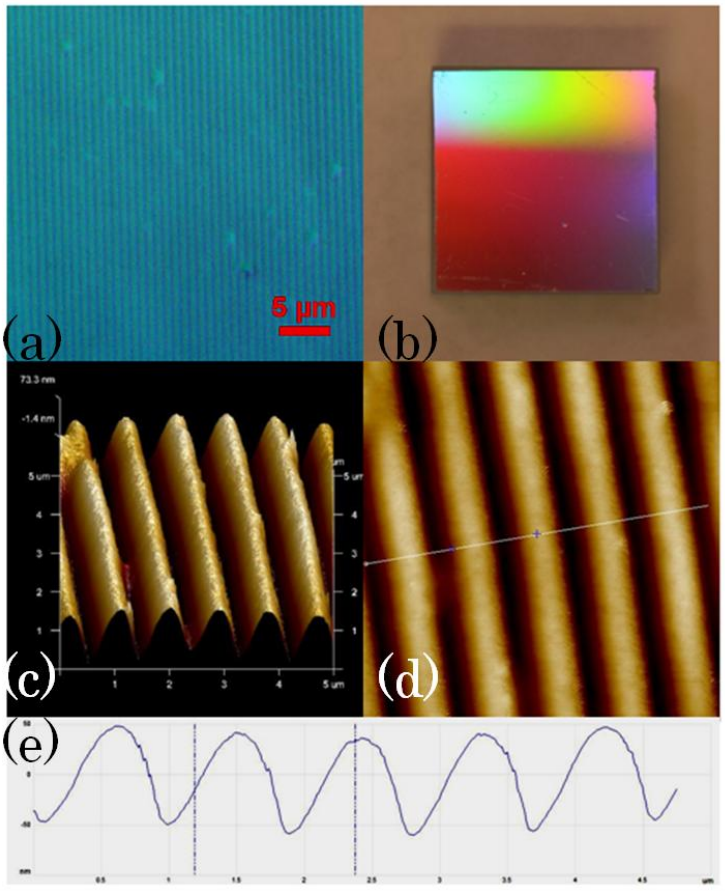


Figure 6. The PDMS Grating Samples Prepared Using a Commercial Grating are Shown in the Optical Image (a), and the Atomic Force Microscope Images (c) and (d). The Grating Samples are Fabricated by Using a Commercial Grating as a Mold. The Commercial Grating is Shown in (b). (e) is the Height Profile along the Cutline in (d).

3.2 PDMS Effect

The change in measured diffraction angle directly relates to the change in periodicity of the PDMS/Au grating. One glaring question that needs to be answered is whether or not the strain on the grating reflects the underlying strain on the specimen of interest. The commercial finite element package ABAQUS was used to study this effect. Fig. 7(a) shows the model, including a PDMS grating with a thickness of 100 μm and length L on top of a 0.5 mm thick, 10 mm long silicon substrate. Thermal stress analysis is conducted by introducing a uniform temperature change $\Delta T$. The PDMS and silicon substrate are modeled by 4-node plane strain temperature-displacement coupled elements (CPE4T). The PDMS-Si interface is treated as shared nodes. The bottom of the silicon substrate is confined. The top Au layer is not considered in the finite element analysis because its thickness is negligible (10 nm). The following material parameters are used in the analysis[96]: $E_{PDMS}$ = 2 MPa, $\nu_{PDMS}$ = 0.5, $\alpha_{PDMS} = 310\times10^{-6}$ /°C, $E_{Si}$ = 130 GPa, $\nu_{Si}$ = 0.3, $\alpha_{Si} = 2.6\times10^{-6}$ /°C, $T$ = 50°C, where $\alpha$ is the coefficient of thermal expansion (CTE).

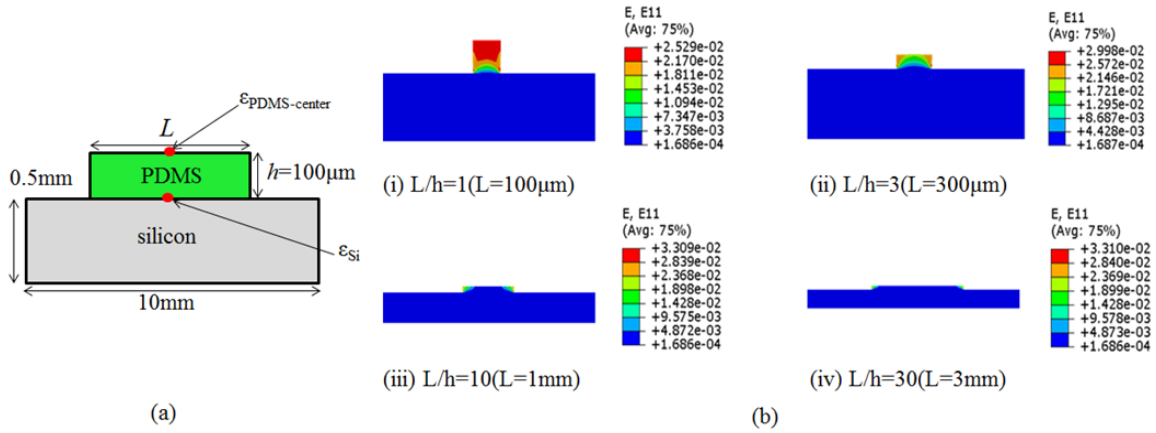


Figure 7. (a) Schematic of PDMS Grating Attached on Silicon Substrate. (b) Strain Contours in the Horizontal Direction for Different ratios of PDMS Lengths ($L$) and a Constant Thickness ($h$ = 100 μm).

Strain contours in the horizontal direction for different ratios of PDMS length and thickness are shown in Fig. 7(b). For $L/h$ = 1, the strain at the top surface of the center of the PDMS ($\varepsilon_{PDMS}$) is about two order of magnitude higher than the strain at the top of the silicon substrate ($\varepsilon_{Si}$). The explanation for this is that for a small $L/h$ ratio, the constraint from the underlying silicon substrate is too weak. Therefore, the strain at the top of the PDMS grating, in this case, only reflects the PDMS itself and not the underlying silicon. As the $L/h$ ratio increases, the constraint from the silicon substrate is increased and the strain at the top of the PDMS grating begins to resemble more and more like the strain of underlying silicon specimen of interest, as can be seen in Fig. 7(b). For an $L/h$ ratio of 30, the strain of the PDMS grating is equal to the strain of the underlying silicon specimen of interest over 80% of the entire surface area of the PDMS grating. In this scenario, the detected strain $\varepsilon_{PDMS}$ reflects the actual strain $\varepsilon_{Si}$.

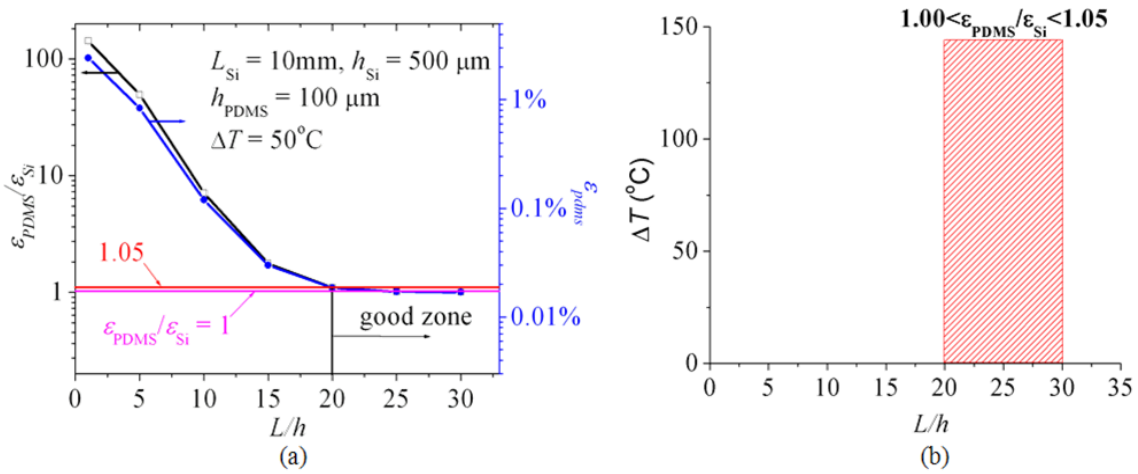


Figure 8. (a) $\varepsilon_{pdms}/\varepsilon_{Si}$ and $\varepsilon_{pdms}$ as a Function of L/h. (b) Phase Diagram of $\varepsilon_{pdms}/\varepsilon_{Si}$.

Figure 8(a) shows the ratio of $\varepsilon_{PDMS}$ and $\varepsilon_{Si}$ as a function of $L/h$ ratio for PDMS grating on Si substrate. It can be seen that when the $L/h$ ratio exceeds a critical value of 20, the $\varepsilon_{PDMS}$ reflects $\varepsilon_{Si}$ with only a 5% error. Fig. 8(b) shows that this relation (i.e., $L/h$ > 20) holds for all temperature change due to the linearity of this relation. In fact, this analysis is likely to provide an upper bound of the $L/h$ ratio because the CTE mismatch between silicon and PDMS is likely to be more severe than most conventional metals and polymers. However, note that for materials with a smaller CTE than silicon, such as, glass and other low CTE ceramics, the critical value for $L/h$ ratio can be smaller than 20.

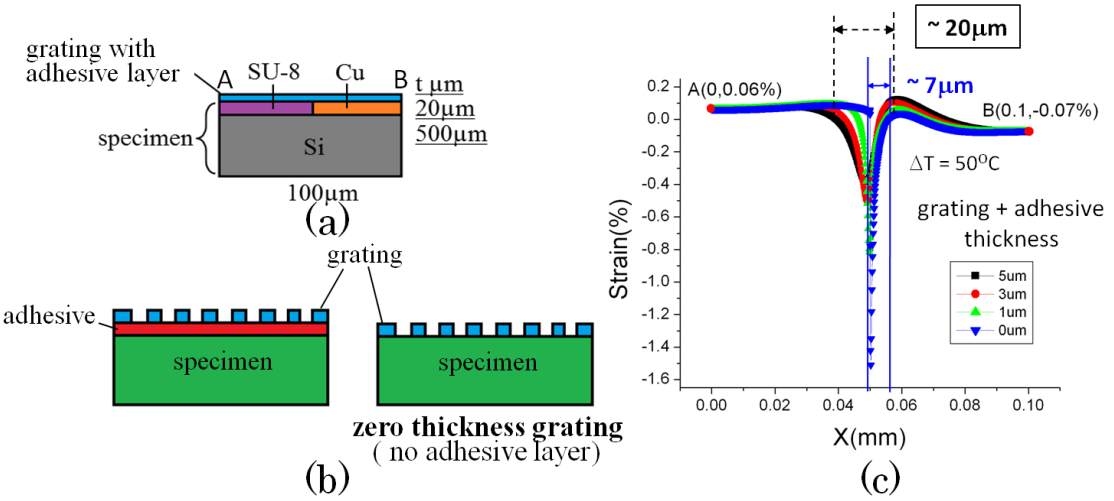


Figure 9. (a) Schematic of a Grating Attached on a SU-8/Cu Composite Specimen. (b) Schematic of a Finite Thickness Grating and a 'Zero-Thickness' Grating. (c) Strain as a Function of the Horizontal Distance on the Top of the Grating. Here the Temperature Change $\Delta T$ is 50 ˚C.

Although we want to measure the strain of the surface of the specimen, we actually measure the strain of the surface of the specimen grating. The difference can be very significant when it comes to micro-mechanics analyses for a composite specimen. Finite element analysis is used to simulate the thermal deformation scenario. A grating is attached on top of a SU-8/copper composite, which is mounted on a silicon substrate, as shown in Fig. 9(a). When subjected to a temperature change, we expect that the junction experiences a sudden strain change due to the CTE mismatch between SU-8 and copper. By varying the thickness of the grating from 0 to 5 μm, the strain distribution on the grating surface is calculated as plotted in Fig. 9(c). It is observed that when the grating thickness is zero there is a sharp jump of strain over a range of 7 μm long (blue curve).

When the grating thickness increases to 5 μm, the strain only jumped a little bit over a much wider range 20-μm-long (black curve). Obviously, finite thickness grating will smear out the strain information from the specimen as strains are attenuated and redistributed when transmitting through the grating thickness, which is known as shear lag effect[97]. Therefore, there is a need for zero thickness gratings fabricated on specimen to reflect the real strain on specimen as shown in Fig. 9(b).

### 3.3 Zero-Thickness Gratings

One method is the direct fabrication of zero-thickness gratings using soft contact lithography[98]. The soft contact optical lithography uses a PDMS mask instead of a glass mask that is traditionally used in photolithography to create the underlying pattern, as illustrated in Fig. 9. The pattern is created due to the difference in light intensities in areas where there is direct contact between the mask and substrate and areas where there is not direct contact. The areas in direct contact with the mask get exposed much more by the light than areas where there is no contact which is why a pattern is created. The exposure source is a 365 nm UV lamp instead of a traditional mask aligner which further reduces the cost. Resulting patterns generated by this technique are shown in Fig. 10. This low cost, easy-to-implement direct grating fabrication technique is very important for potential end users of tunable grating strain sensor, where sub-micron gratings are routinely needed for each sample analysis and yet very little lithography tools are needed.

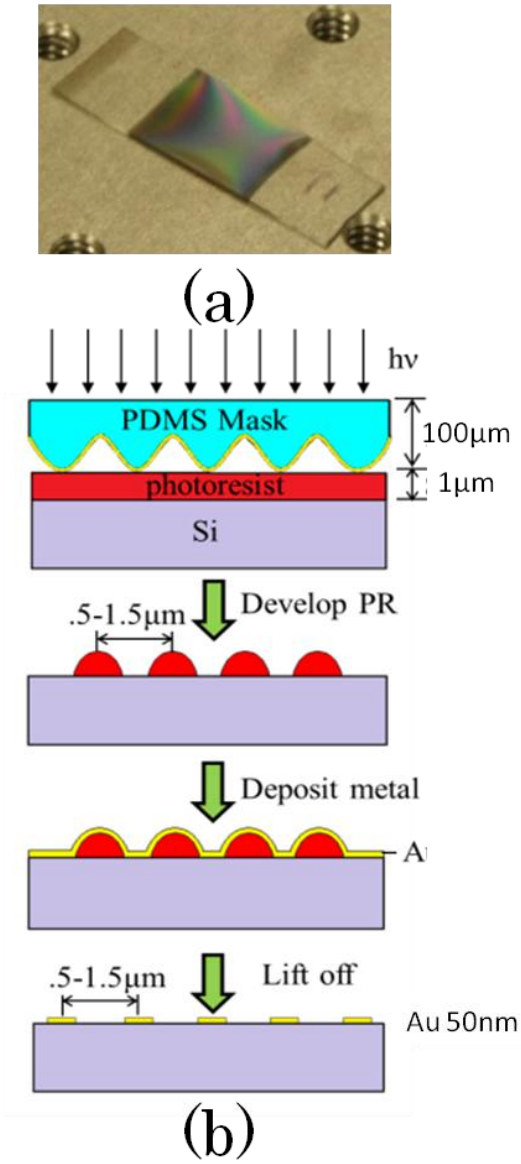


Figure 10. (a) PDMS Grating Utilized as the Photo Mask. (b) Process Flow for the Direct Fabrication of the Zero-Thickness Grating through Soft Contact Lithography.

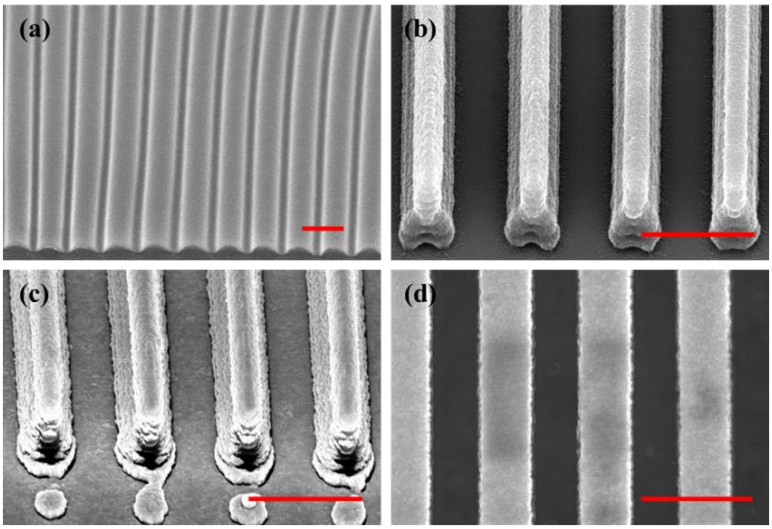


Figure 11. SEM Images of (a) the PDMS Grating Mask; (b) Grating Lines after Photolithography and Development; (c) Grating Lines after Metal Deposition; (d) Grating Lines after Lift-off.

Also electron beam lithography (EBL) is utilized in creating continuous domains of gratings with slightly changed periodicities on the same substrate. Fig. 12 displays the schematic of applying EBL to create periodic lines, which is from the Springer handbook. EBL gives flexibilities in pattern design and is able to create gratings with precise periodicities. This helps to design simplified models for strain sensing method verification. The details will be discussed later.

Grating patterns fabricated on the microelectronic packages are using focused ion beam (FIB) for good quality. Since the grating patterns are fabricated on the cross-section of the electronic package, it is difficult to spin-coat photo-resistor onto the target substrate. Therefore, FIB is a better solution to fabricate high quality gratings than EBL.

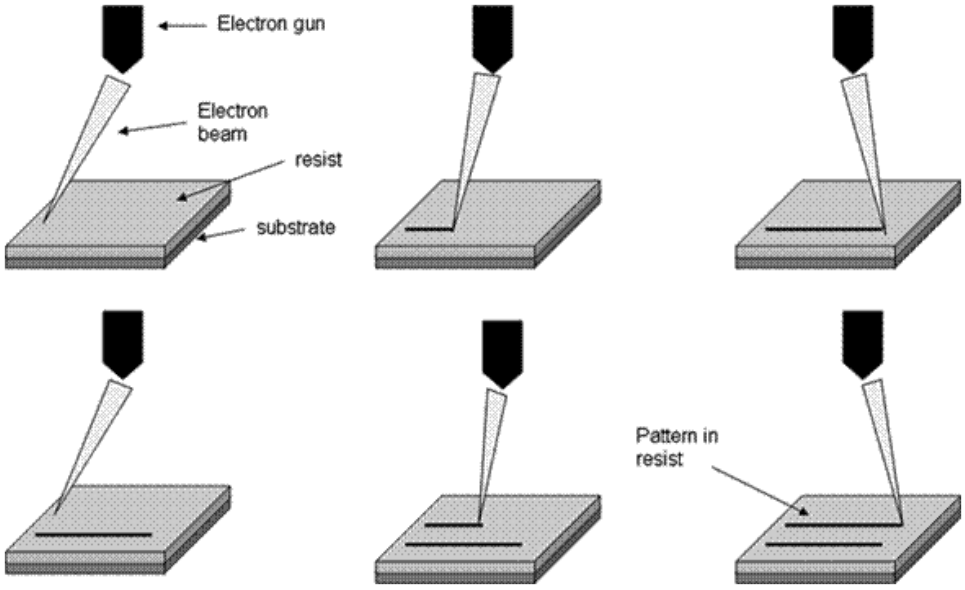


Figure 12. Schematic of EBL Writing Patterns.

CHAPTER 4

Optical Testing Setup

## 4.1 Testing Setup

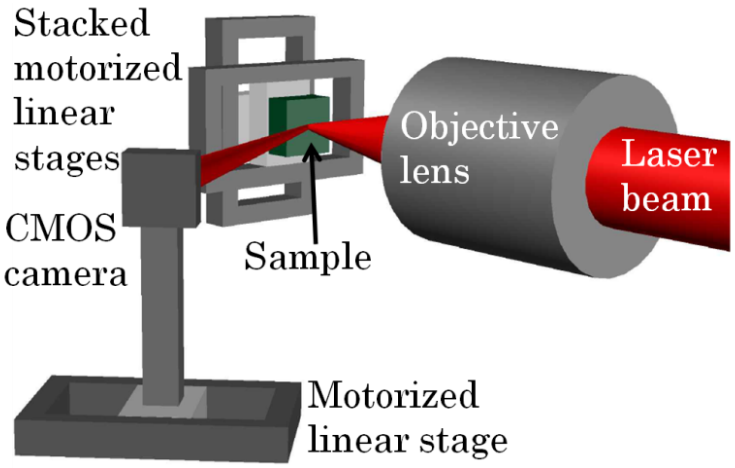


Figure 13. Schematic of the Optical Setup.

The schematic of the optical setup is shown in Fig. 13. The incident laser is a single mode, linearly polarized HeNe laser with an output wavelength of 633 nm and an output power of 21 mW. A CMOS camera (DCC1545M from Thorlabs. Inc) is mounted on the motorized linear stage to capture the diffraction signal profile. The sensing area of the CMOS camera is 6.66 mm by 5.32 mm. The pixel size is 5.2 μm by 5.2 μm. It is mounted on a motorized linear stage which has a traveling distance of 1 inch. The camera is set to take 4 pictures while the motorized linear stage travels its full range. By combining the 4 pictures, one is able to track up to 1 inch of the diffraction peak shift at the camera side. The camera is placed around 10 cm away from the testing sample. The sample is mounted on the diagonally stacked motorized linear stages for 2D scanning capability. The range for both stages is 1 inch, which sets the maximum field of view for

the strain mapping to be 1 inch by 1 inch. The motorized linear stages have a minimum increment of 0.1 μm, which is sufficient for the spatial resolution study in this work, where the smallest step size is set to be 1 μm during the measurement. A LabVIEW program is used to automate a system that controls the two-dimensional sample scan, camera motion, and data acquisition.

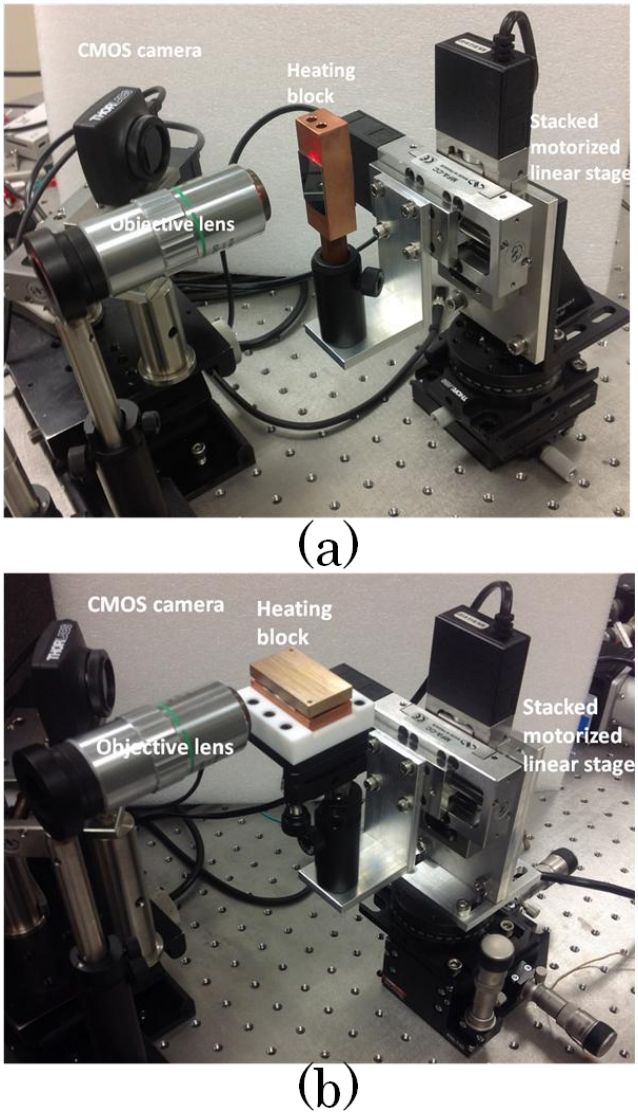


Figure 14. Testing Setups. (b) is Designed for Cross-Section Samples.

The heating setups are presented in Fig. 14. In this work, the setup in Fig. 14(a) is to test homogeneous samples and the SU8/Si composite sample. To test the cross-section of the microelectronic package, the setup displayed in Fig. 14(b) is applied. The sandwich structure of the heating blocks helps to elevate the temperature up to ~180°C.

## 4.2 Experiment Procedure

The first step is to adjust the alignment. Initialize all the motorized linear stages through LabVIEW user interface. Then the laser source is turned on and the laser beam hits the sample surface. Adjustments are made in the tilting of the sample to ensure that the incident laser beam is normally incident on the sample surface. In order to adjust the incident light tilting, one can place a half-transparent screen in front of the sample, and observe the incident light spot and the reflect light spot on the screen. Then adjusting the tilting of the sample to ensure that the observed two spots are overlapping.

The second step is to perform the calibration for the diffraction angle versus the diffraction peak position relationship. In order to perform this calibration, the sample holder must be placed on a rotational stage. Then the rotational stage is rotated by a known angle and a scan is performed so that the photodetector can capture the diffraction signal profile via the LabVIEW program. The beam profiles for a set of angles are then recorded. The data set will be processed by the MATLAB program to extract the relationship between the diffraction angle and the diffraction peak shift. Whenever the testing setup is adjusted, or the testing temperature is changed, this calibration has to be conducted.

The laser spot is then moved to the starting point of the interested scanning area, and the scanning conditions are defined in the LabVIEW GUI. The experimental data is saved as sets of text files and can be further processed by the MATLAB program.

CHAPTER 5

Software

## 5.1 Automation

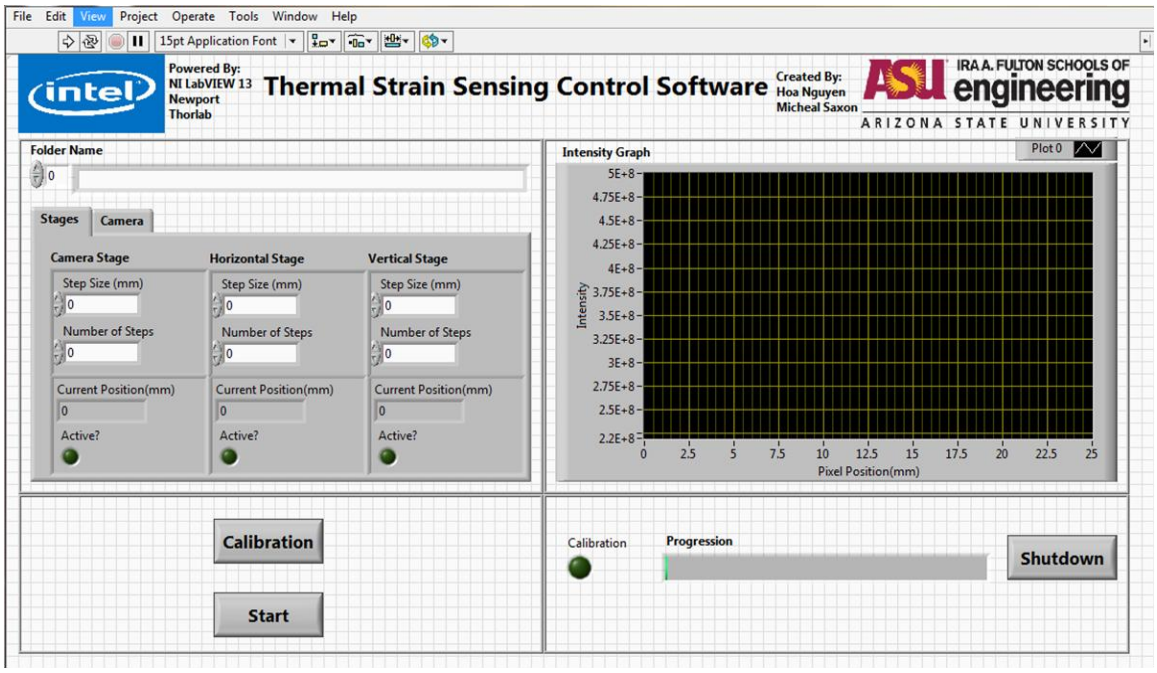


Figure 15. LabVIEW Graphic User Interface (GUI) for the Automation Control.

The automation of the strain sensing measurement is controlled by the LabVIEW program. As shown in the captured graphical user interface (GUI), the program is integrated with the user defined step sizes and scan ranges for the horizontal and vertical sample stage scans, together with the parameters to set up the camera stage scan. The displayed graphic window is to present the real time diffraction signal profiles captured by the camera for each sample position. The LabVIEW program has been improved by utilizing the state machine structure, in order to ease the effort for regular maintenance and increase the extendibility.

The 'calibration' button displayed in Fig. 15 is to take a room light picture without incident laser for reference, in order to improve the signal to noise ratio. Since the sensing area of the CMOS camera is 6.66 mm by 5.32 mm, it is typically set to take 4 images for the camera to cover 1 inch range which is the full traveling range for the motorized linear stage. The four images are combined to display the complete diffraction signal profile, at the real-time 'Intensity Graph' window and in the output text file. The displayed 'Intensity' (vertical axis) is the sum of the captured signal along each column of the camera. The displayed horizontal axis is the position along the camera scan direction. Therefore the output text file includes two columns of the data, one is for the 'camera position', which has a total range of around 1 inch with a step size of 5.2 μm (related to pixel size); the other is the light intensity, which is the sum of the sensed light intensity in the entire column. For a one dimensional scan, the output files are a series of text files named as the 'measurement#', which is related to the # of steps. For a two-dimensional scan, a folder will be created for each vertical sample position. The within the folders, there will be the series of one-dimensional sample scan data, in the horizontal direction.

The testing time is dependent on the total steps defined for the entire scan. If a one-dimensional scan in horizontal direction is set to have a step size of 5 μm and 100 steps, it will take about 30 minutes to complete the scan. A potential solution to reduce the testing time is to replace the current CMOS camera to a camera with a larger sensing area, so that no scan of the camera is necessary to capture the diffraction signal profile. In this case, the testing speed will be significantly increased.

## 5.2 Data Analysis


Figure 16. MATLAB GUI for the Data Analysis.

The experimental data are processed by the MATLAB program. It is developed to process the text data files from the previous LabVIEW program for calculations and generation of graphs. It is capable of depicting contour plots for one-dimensional scan and perform Gaussian fit for the selected range of the data files.

To start the data process, the first step is to process the calibration of the diffraction angle versus diffraction peak position relationship at the beginning. Fig. 17 shows an example of the diffraction angle calibration result. The vertical axis displays the position at the camera, which ranges from 0 to 1 inch. The horizontal axis is the diffraction angle. The blue dots are the measurement results from the calibration (as described in Chapter 4.2 for the procedure), while the red line the linear fit for the blue dots. The equation displayed in the plot expresses the relationship between the camera position and the diffraction angle, and serves as the reference for translating the peak position at the

camera side into the grating wavelength. Whenever a new calibration file is run by the MATLAB program, the equation will be updated for the MATLAB code for further plotting and calculation.

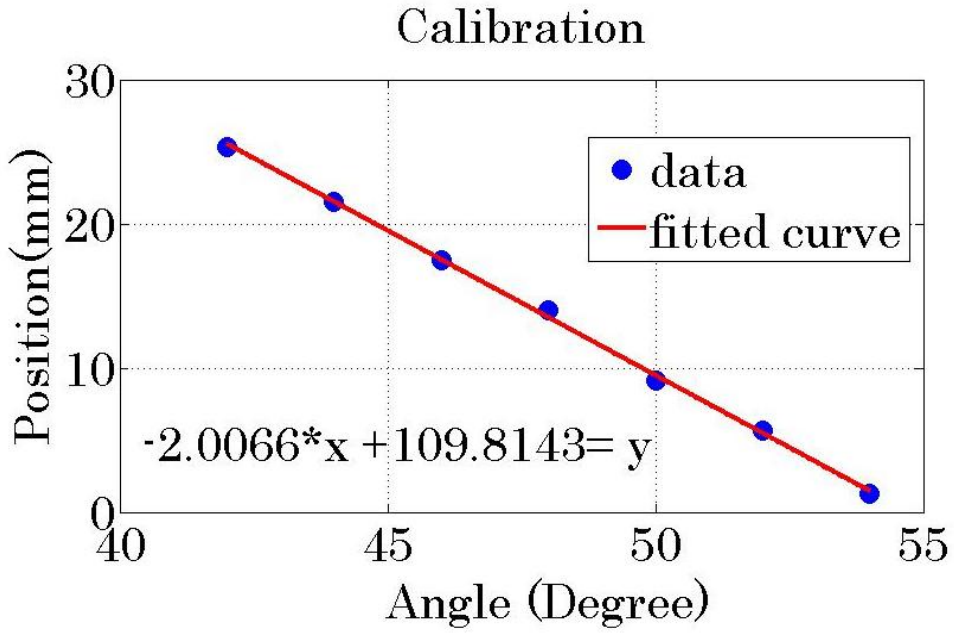


Figure 17. Calibration of the Position (at the Camera Side) versus the Diffraction Angle (in Degrees).

Then the loaded data series for each scan can be depicted as the contour plots. Meanwhile, the 'diffraction peak position versus sample position' text file is generated simultaneously for plotting two-dimensional contour plot. In addition, it is built in with the option of generating 'linear' or 'log' contour plot and the capability of configuring the display range of the y-axis, for better interpretation of the data. In some cases, the grating wavelength information is extracted by fitting method. Hence the MATLAB program is

integrated with the functionality to smooth the data, perform Gaussian fit and present the extracted grating wavelength.

The two-dimensional contour plot is generated by the following MATLAB code.

MATLAB code:

```
clc
clear all
x = [];
y = [];
z = [];
vertical_step = 5; % change this number according to vertical step (i.e 10um will be 10)
horizontal_step = 3; % change this number according to horizontal step (i.e 10um will be 10)
directory = 'F:\Hannah_D\MATLAB\9_12_2014_Intel sample_3um_scan16_bot24um'; %change the name of the directory of the folder you want to graph
path = dir(directory);
cell = struct2cell(path);
length = length(cell);
hold on
for i = 3:length
  data = load(strcat(directory,'\',cell2mat(cell(1,i)),'\Sample Position(mm) vs. Wavelength(nm).txt'));
   x = (0:horizontal_step:3*(size(data,1)-1))';
```

```
    y = (i-3)*vertical_step*ones(size(data,1),1);
    z = data(:,2);
    mesh([x';x'],[y';y'],[z';z'],'mesh','column','marker','.','markersize',50); % This number 20
change the size of the circle
end
colorbar
axis([-1*horizontal_step size(data,1)*horizontal_step -1*vertical_step
vertical_step*(length-2)])
xlabel('Horizontal Sample Position(um)','Fontsize',24);
ylabel('Vertical Sample Position(um)','Fontsize',24);
title('Scan 16','Fontsize',24) %name of the graph
ylabel(colorbar,'Grating Wavelength(nm)','Fontsize',24);
set(gca,'Ydir','reverse') % This line will reverse the y-axis. put % in front of the line if
you don't want y to be reversed
set(gca,'fontsize',20)
hold off
```

CHAPTER 6

Experimental Results

## 6.1 Strain Sensitivity Validation

Thermal strain of PDMS, copper and silicon were measured by employing the PDMS grating onto the target substrates. PDMS/Au gratings are bonded on specimens that are heated up by a copper block, as shown in Fig. 14. A thermal couple is attached to the copper block to form a feedback system for the temperature control. In this system, the temperature reading on the specimen is calibrated to be within one degree of accuracy, and the temperature range for the strain measurement is between 20 °C and 65 °C. The laser spot size is 200 μm.

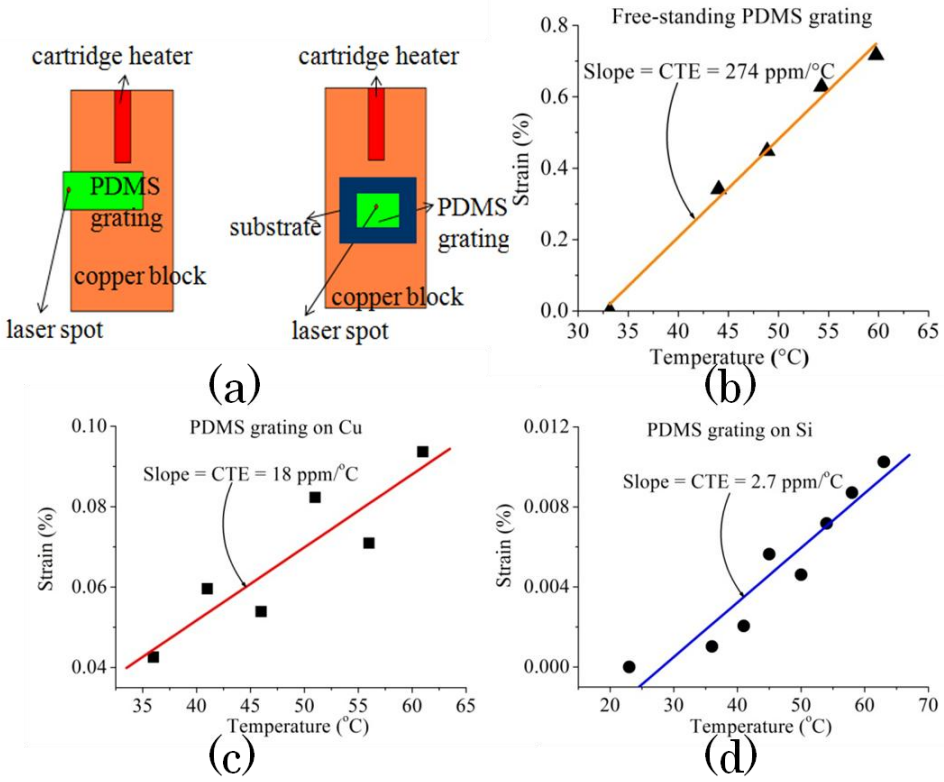

Figure 18. (a) Schematic of the Testing Setups. CTE Extractions for (b) Free-Standing PDMS, (c) Copper and (d) Silicon.

The first specimen is a free-standing PDMS grating, which is hanging over at the edge of the copper block, as shown in the left schematic in Fig. 18(a). The focused laser spot is located just off the copper block to measure the thermal strain of the PDMS grating without constraints from the copper block. Fig. 18(b) shows the measured strain as a function of temperature for this free-standing PDMS grating, where a good linearity is observed. The extracted CTE of PDMS, which is presented as the slope of the strain versus temperature in the data plot, is 274 ppm/°C (part per million per degree Celsius). The measurement data agrees well with the reference value of the CTE of PDMS, 265 ppm/°C, measured commercial thermal-mechanical analysis tool Q400 from TA instruments, under expansion mode at 10 mN force.

The second specimen is a copper block, on which the PDMS/Au grating is attached by a thin double-sided adhesive tape. The size of PDMS/Au grating has been chosen based on Fig. 8 to ensure the measured strain on top of the grating accurately reflects the strain of copper substrate. Fig. 18(c) shows the strain-temperature relation. The CTE of copper given by the slope is obtained as 18.2 ppm/°C, which is consistent with the CTE value of copper (17.5 ppm/°C)[99]. Some of the data points in Fig. 18(c) are scattered compared to Fig. 18(b), which can be attributed to the bonding quality of the adhesive tape between copper and PDMS.

The last specimen is a Si substrate. The PDMS/Au grating can be firmly bonded to the Si substrate by treating the Si surface with oxygen plasma to form a $SiO_2$ bond

between the PDMS and Si[100]. Si has a much lower CTE (2.6 ppm/°C), compared to previous two specimen materials. The experimental data is plotted in Fig. 18(d), which gives an extracted CTE value of 2.73 ppm/°C, very close to the reference value of the Si CTE. The measured data here show much less fluctuation than the data from the PDMS bonded to copper as the result of much better bonding quality between Si and PDMS. Since the temperature is raised by 5°C, the smallest strain differentiated from the test is 10 micro-strain. Thus the high strain sensitivity of the developed strain sensing technique is validated.

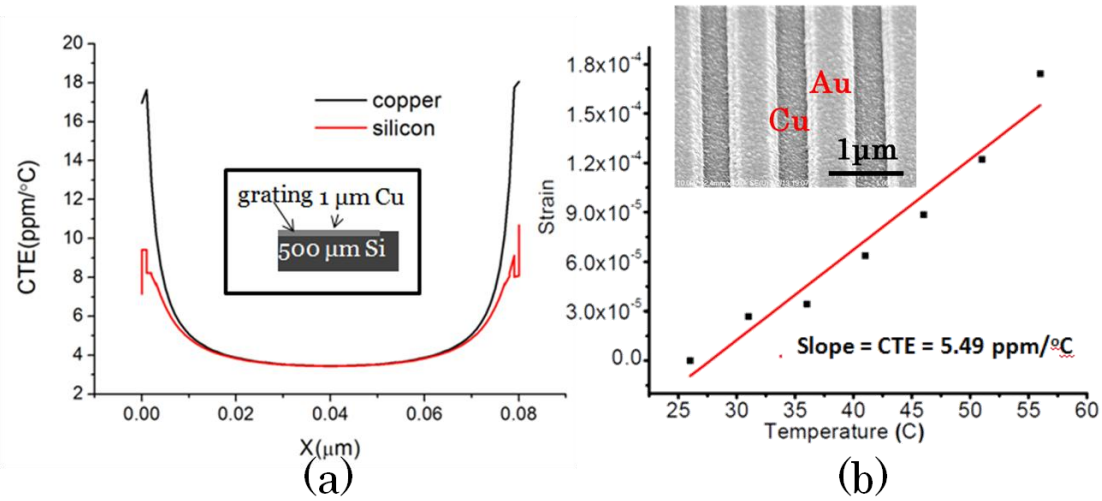


Figure 19. (a) Simulation Results of Strain Distribution for Thin Copper Layer on Thick Silicon Substrate. (b) The Extracted CTE Value is Between the CTEs of Copper and Silicon.

Thermal strain measurements were also conducted on the samples with gold grating fabricated on the electroplated copper substrate, as shown in Fig. 19(b) inset. The thickness of copper layer is 1 μm. It is electroplated on Si wafer which has a thickness of

500 μm. The simulation work (Fig. 19(a)) clearly indicates that the copper layer experiences a strain constraint from the underlying Si substrate, where the closer to the center the spot is, the stronger the constraint is. The measurement data fall in the range of around 5-12 ppm. The data plotted in Fig. 19(b) suggest a measured spot relatively close to the edge.

Thermal strain measurements on homogeneous materials, especially for silicon achieve good experimental results compared to the reference data. The strain measured from silicon sample is on the order of 10 micro-strain scale, thus demonstrating the high strain sensitivity of the technique.

Other than the strain sensitivity, the other primary goal for development of the strain sensing technique is to achieve strain mapping of the electronic packages under increased working temperature with high spatial resolution and simultaneously keeping a large field-of-view. Incorporation of the motorized linear stages into the optical setup grants the scanning capability of the samples for strain mapping. The parameters that affect the spatial resolution of our micro-strain sensing technique significantly include laser spot, laser wavelength, grating periodicity, sample scanning step size, and etc.

## 6.2 Spatial Resolution Investigation

Two types of grating patterns are designed for the spatial resolution study. Single domain patterns are designed to observe resolvable signals from different domain sizes. Given a fixed laser output power and laser spot size, fewer grating lines result in a weaker and broader diffraction signal. The multiple-domain patterns are designed to

observe shifts in the peak position. Different laser spot sizes result in different appearances of the diffraction signal in the contour plot. Therefore, different extraction methods are applied to calculate the grating wavelength for each domain.

The one dimensional scans are first performed on single domain patterns. Experimental results reveal that the incident laser spot size affects the outcome of the contour plots which is observed in the diffraction signal. Different extraction methods for calculating the grating wavelength information are developed by inspecting the different laser spot size cases.

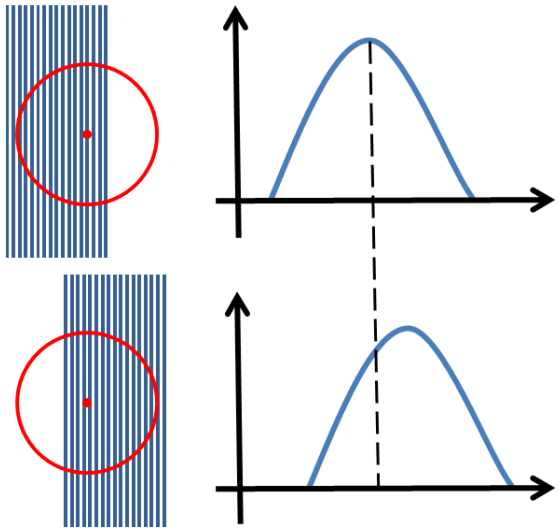

Figure 20. Schematic of the Diffraction Signal Profiles at Two Sample Positions with a Larger Laser Spot Size than the Domain Size.

We first need to understand the laser scanning process for strain mapping using fabricated grating patterns on samples. As shown in the schematic in Fig. 20, the sample is moved from the left to right following the motion of the linear stage, while the laser

beam is fixed. The camera captures two independent Gaussian shape diffraction signals for the corresponding sample positions. Although the grating period remains unchanged, the captured diffraction signal at the camera is shifted in the horizontal direction, which is calculated as a diffraction angle variation. Hence, the presented peak shift is an artificial effect coming from the scanning behavior when the laser spot size is larger than the domain size, even though the diffraction angle still follows the grating equation and keeps the same value. However, the effective laser spot center point shifts because of the Gaussian energy distribution of the laser beam. And this effective laser spot motion is reflected at the camera as additional peak shifting. Therefore, it is necessary to apply corrections to the data processing in order to extract accurate grating wavelength information without this artificial effect due to sample position change.

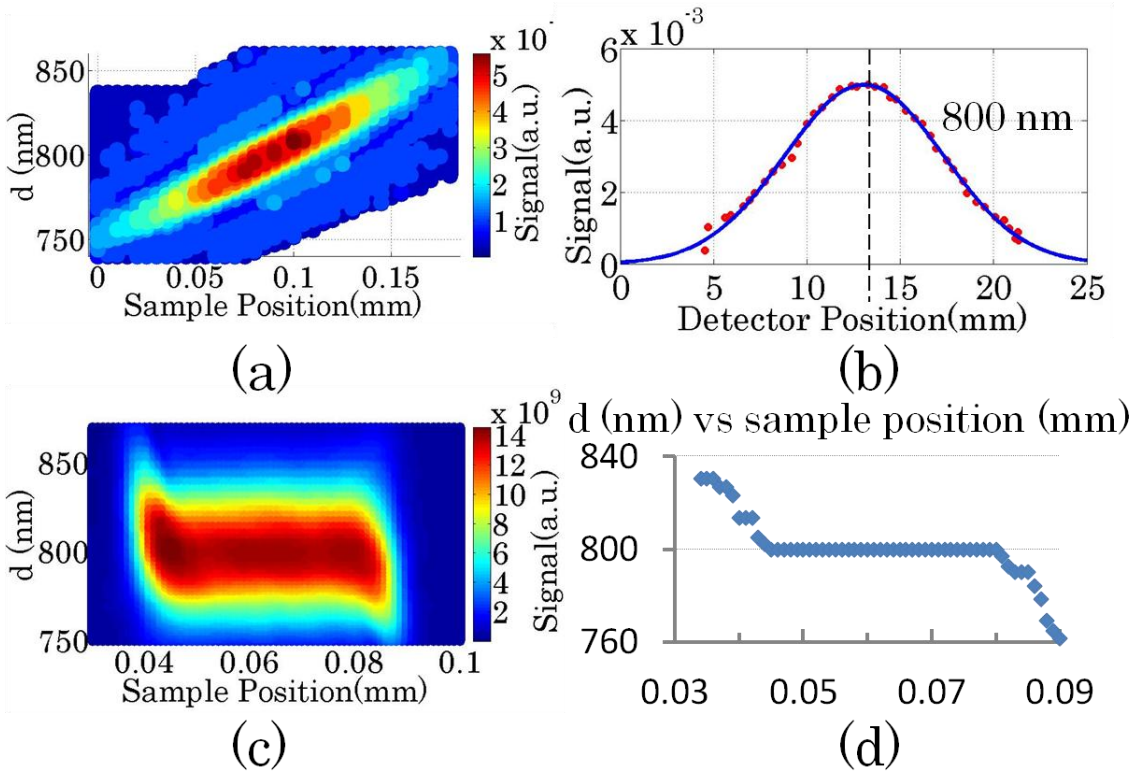

Figure 21. (a) and (c) Contour Plots of 1D Scans across the Single 50 μm Domain Pattern, with a 100 μm Laser Spot Size and a 20 μm Laser Spot Size Respectively.

The contour plot shown in Fig. 21(a) is the measurement results from a one-dimensional scan on the single 50 μm domain pattern with a 100 μm diameter laser spot size. During the measurement, the incident laser beam position is fixed, while the sample is automatically moved from left to right with a controlled step size. The scanning results are plotted in the contour plot (left), while the right plot shows the data extraction process. As mentioned above, the laser beam has a Gaussian profile, which causes the effective laser spot position to be shifted when different parts of the laser are shined on the grating pattern. Consequently, it adds additional shifting to the diffraction peak displacement at the camera, and exhibits variations in the diffraction signal intensity. The setup only exhibits zero additional peak shifting and reaches maximum intensity when the center of the laser spot aligns with the center of the domain. This allows for an accurate grating wavelength to be calculated from the measured domain. As illustrated in Fig. 21(b), at each sample position (on the x-axis of the contour plot), the peak position and intensity of the diffraction signal was extracted and plotted as a red dot. A complete 1D scan gives a series of red dots. By performing a Gaussian fit, one can find the corresponding detector position for the diffraction peak maximum and calculate the grating wavelength. 1D scans have been conducted on a single domain patterns with domain widths of 50 μm, 20 μm and 10 μm, respectively, which have been accurately

resolved with the current setup. Fig. 22 presents the contour plots for the 1D scans across the single 20 µm domain and the single 10 µm domain. The extracted grating wavelength are consistent with the designed grating wavelength of 800 nm.

A separate 1D scan on the same single 50 µm domain pattern has been conducted with a laser spot size of 20 µm in diameter, which is smaller than the domain size. The results are graphed in the contour plot shown in Fig. 21(c). In this case, the extracted grating wavelength versus the sample position curve shows a constant region in the center of the domain, where it suggests that the artificial shift does not occur for that region since the laser spot size is smaller than the domain size. The actual grating wavelength information can be directly read out from the constant region of the d versus sample position graph without applying fitting procedure to correct the data. Besides that, there are additional shifts evident at both edges of the domain, which do not affect the grating wavelength extraction in this case.

Comparing the contour plots for both cases, the diffraction signals present different outcomes. A smaller laser spot size allows a direct extraction of the grating wavelength information. A larger laser spot size generates a set of data that needs extra data analysis to reveal accurate information out of the raw.

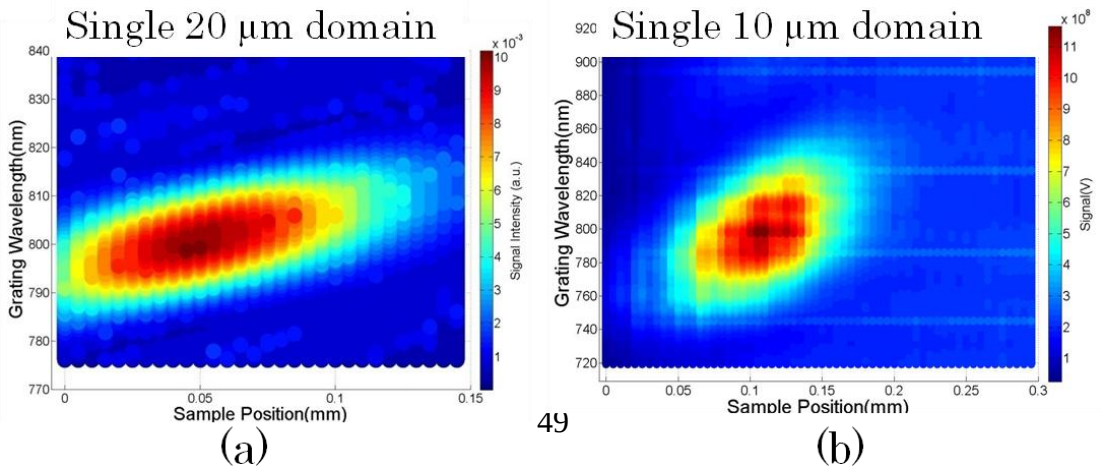


(a) (b)

Figure 22. Contour Plots of 1D Scans across (a) the Single 20 µm Domain Pattern and (b) the Single 10 µm Domain Pattern.

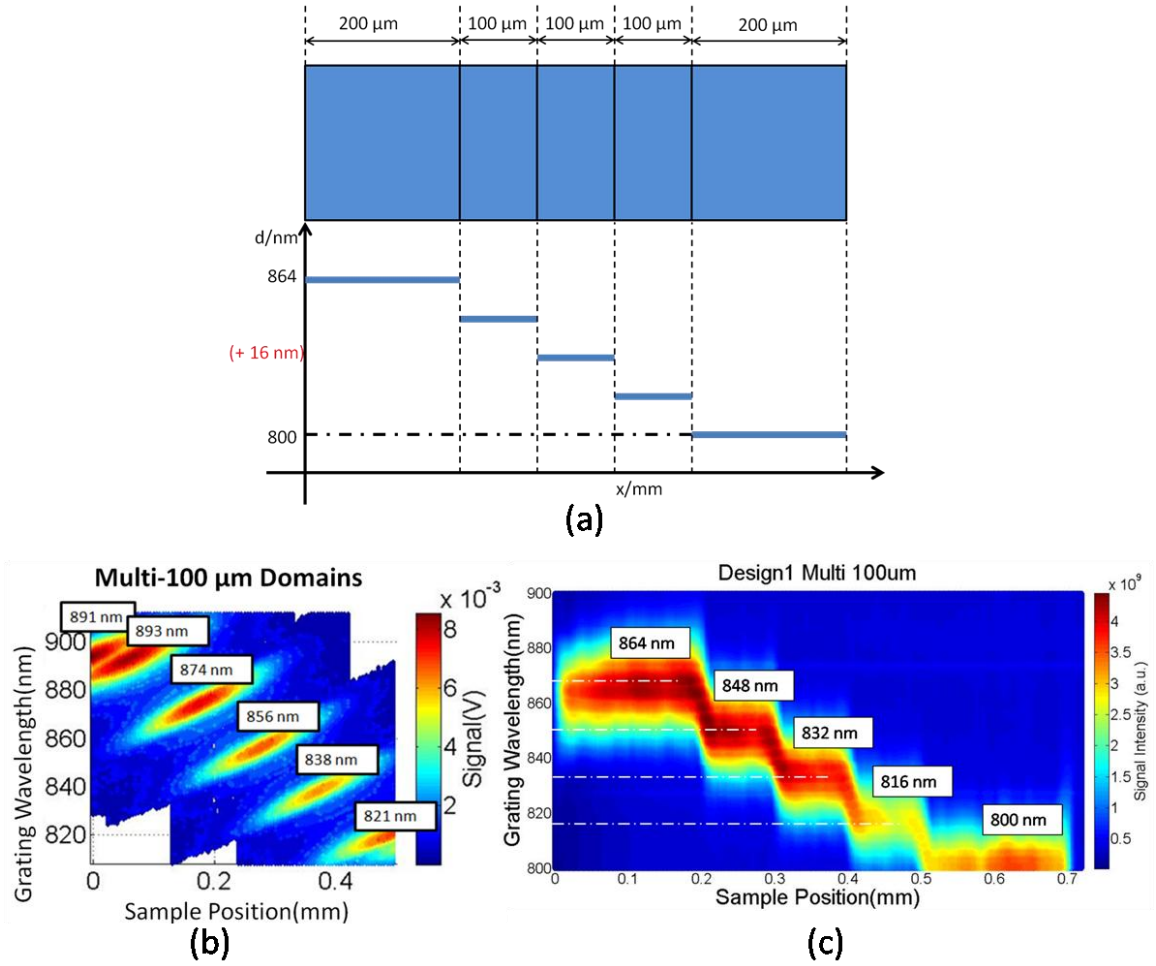


Figure 23. (a) Schematic of the Multiple 100 µm Domain Pattern. (b) and (c) Contour Plots of the 1D Scans across the Designed Pattern, with a larger and Smaller Laser Spot Sizes Respectively.

The following samples scanned are fabricated with multiple-domain grating patterns. 1D scans are performed on the samples to map the grating wavelength variation. Similar to the single domain pattern case, it affects the appearance of the diffraction signals whether the laser spot size is larger or smaller than the domain size. As illustrated in Fig. 23(a), the pattern is designed with continuous 100 μm wide domains in the middle and 200 μm wide domains at both ends. The grating period is designed to increase by 18 nm from right towards left. The two contour plots display the results for laser spot size of 250 μm and of 50 μm in diameters. Large laser spot generates a series of tilted elliptical diffraction signals. By performing Gaussian fit, one obtains the grating wavelength information for each domain, which are labeled on the contour plot. It is clearly observed from the contour plot that the diffraction signals are well separated with 18 nm difference in grating wavelength for the adjacent domains. And the extracted numbers are consistent with the designed ones. It is noticed that the left-most domain displays two very close peaks, which repeats through several independent measurements for this pattern. Hence, it is likely to be caused by the imperfections of the grating pattern. With a smaller laser spot size, the extracted grating wavelength versus sample position plot is stepped, which gives direct readout of the grating wavelength as labeled.

As illustrated in Fig. 24(a), the pattern is designed with a continuous 50 μm wide domains starting from the left side and a 200 μm wide domain at the right end. The grating period is designed to increase by 8 nm from the right side to the left side. The two contour plots display the effect of different laser spot sizes. A large laser spot generates a series of tilted elliptical diffraction patterns. By performing a Gaussian fit, one obtains the grating wavelength information for each domain, in a procedure similar to the single

domain wavelength extraction process, which are labeled on the contour plot. It is clearly observed from the contour plot that the diffraction signals are well separated with around an 8 nm difference in grating wavelength for the adjacent domain patterns. The extracted numbers are consistent with the design. With a smaller laser spot size, the extracted grating wavelength versus sample position plot in Fig. 24(d) has clearly shown step-like pattern without any data extraction process, which gives a direct readout of the grating wavelength.

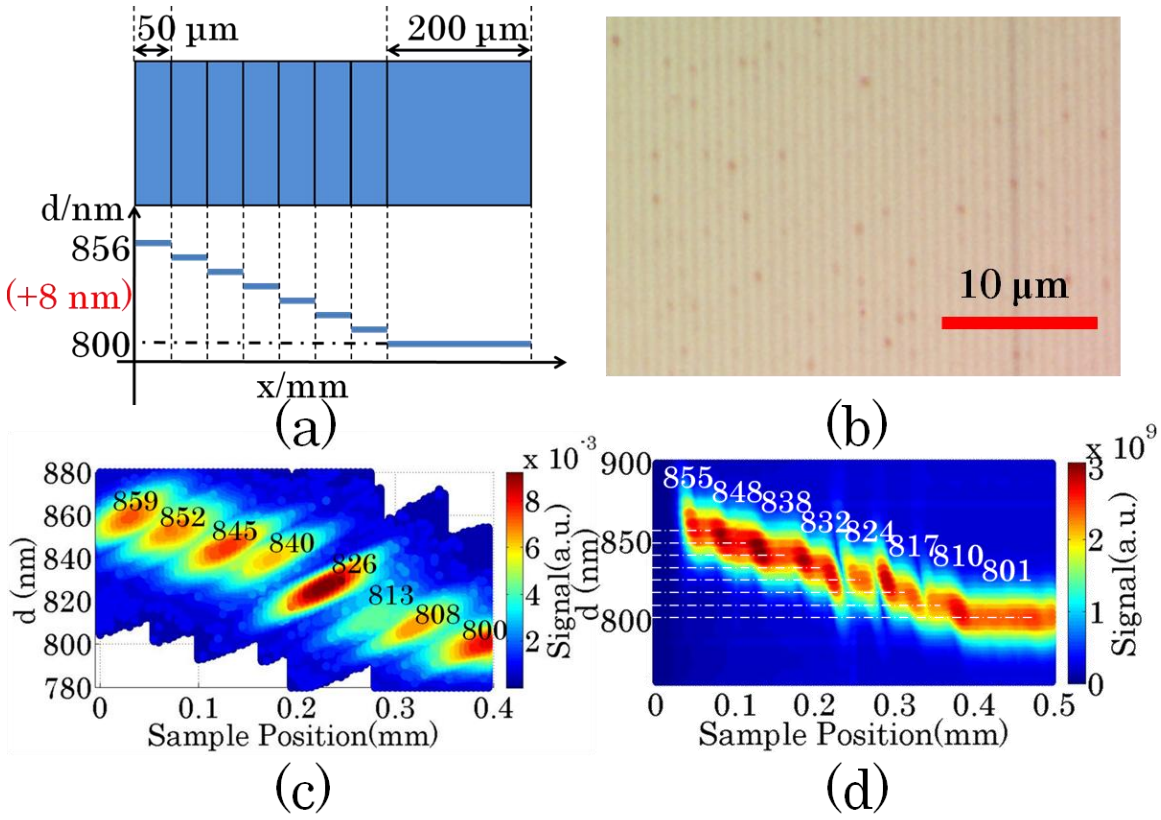


Figure 24. (a) Schematic of the Multiple 50 µm Domain Pattern. (b) Optical Image of the Fabricated Grating. (c) and (d) Contour Plots of the 1D Scans across the Designed Pattern, with a larger and Smaller Laser Spot Sizes Respectively.

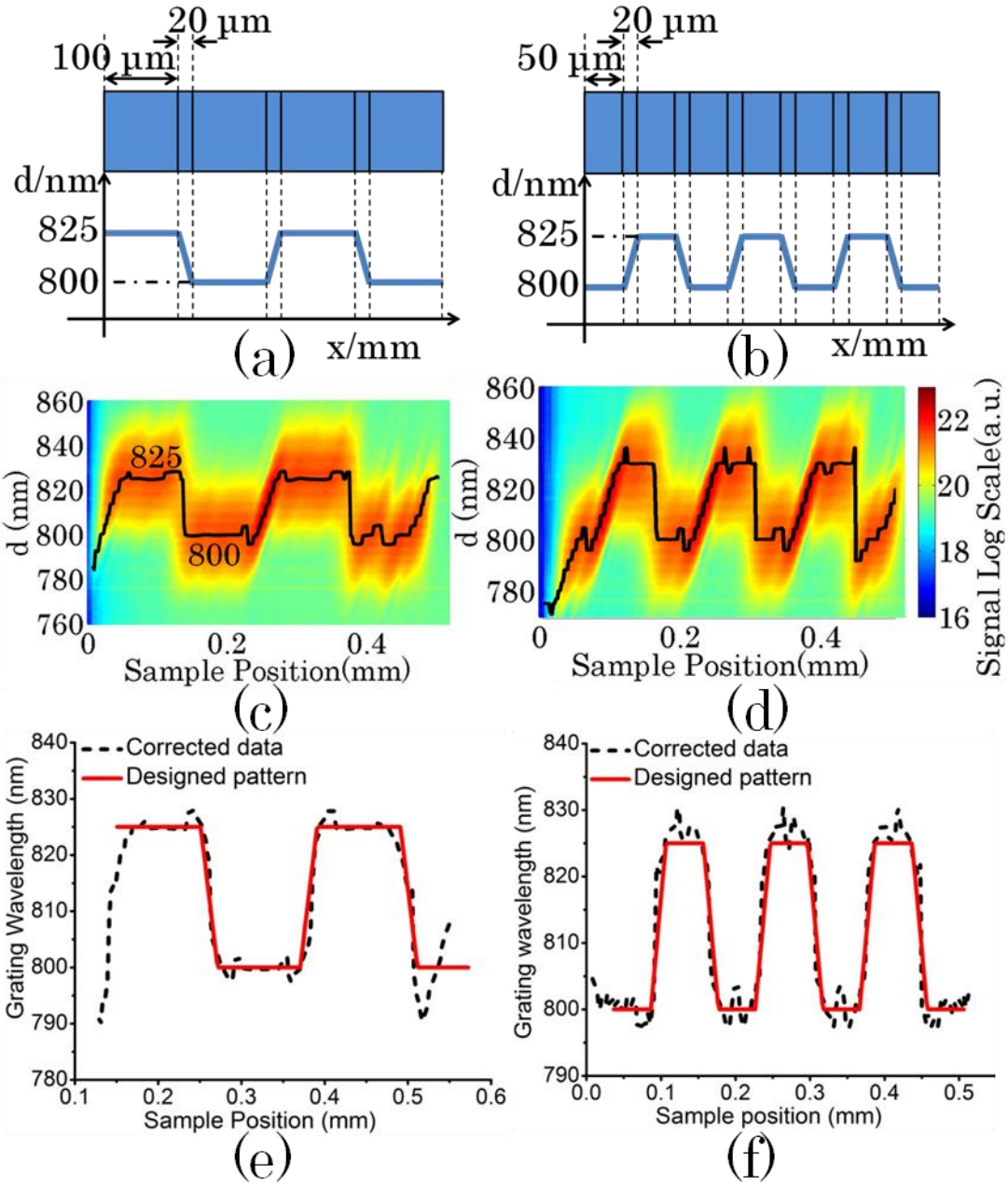


Figure 25. (a) and (b) Schematics of the Multiple Domain Pattern Designs. (c) and (d) Contour Plots Superimposed with the Extracted Grating Wavelength versus Sample Position Curves. (e) and (f) Corrected Experimental Results Compared with the Original Designs.

The following pre-defined EBL patterns are designed to simulate the strain distribution across two dissimilar materials. The experimental work has been presented at the 2014 ECTC conference. When the composite structure is under thermal loading, the two dissimilar materials are expected to expand at different rates according to their CTE values. The strain information is extracted by measuring the grating wavelength variation across the composite sample. In order to model the above case, we defined grating patterns assembled with similar strain variations using EBL, as shown in Fig. 25(a) and (b). In this way, 1D scans under room temperature can be performed to capture the strain variations in order to validate the strain mapping capability for this technique. Gradually changed grating areas are defined at interfaces between two dissimilar materials with a width of 20 μm. The domains are designed to be 100 μm wide (left) and 50 μm wide (right). The laser spot size is slightly smaller than 50 μm in diameter. The designed strain variation is an exaggerated case, since this work focuses on the spatial resolution validation, while the strain sensitivity has been validated in CTE extraction measurements on homogeneous materials.

Contour plots of both patterns are consistent with the designed patterns. The black curves superimposed on the contour plots are the extracted grating wavelength versus the sample position. Since the laser spot size is smaller than the domain sizes, one observes constant grating wavelength regions within the domains whereas the diffraction peak maintains the same position. The extracted grating wavelength variations from both patterns are able to reconstruct the originally designed pattern.

6.3 Strain Mapping on the Composite Sample

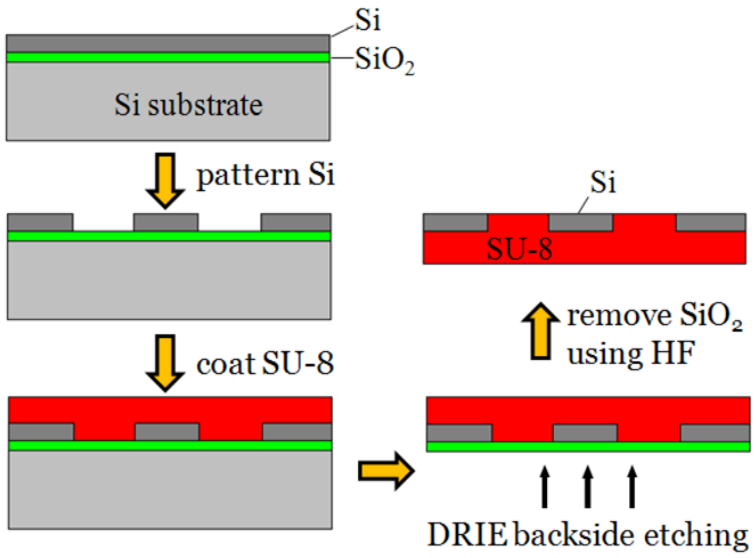


Figure 26. Fabrication Flow of SU-8/Si Junction.

In order to obtain the strain information at the junction of two dissimilar materials with different CTEs upon thermal loading, we fabricated a globally planarized junction composed of SU-8/Si. The fabrication of the SU-8/Si starts from a silicon on insulator (SOI) wafer. The top silicon layer is 10-20 μm thick and is patterned into silicon strips using a standard lithography process. The width of the silicon strips and the spacing are in the range of tens of microns to several hundreds of microns. Then an SU-8 layer is spin-coated on top to fill in the trenches completely. After hard-baking the SU-8 layer, deep reactive ion etching (DRIE) is used to etch the silicon substrate from the backside until the $SiO_2$ etch stop layer, which is then removed at the subsequent step using hydrofluoric acid (HF). Fig. 27 shows the scanning electron microscopy (SEM) image (a) of a SU-8/Si junction and the optical image (b) of a grating on the junction fabricated with EBL. The optical image doesn't focus well for the upper-right-hand corner area

since the junction surface is not perfectly flat and exhibits slight amounts of warping induced by the fabrication process.

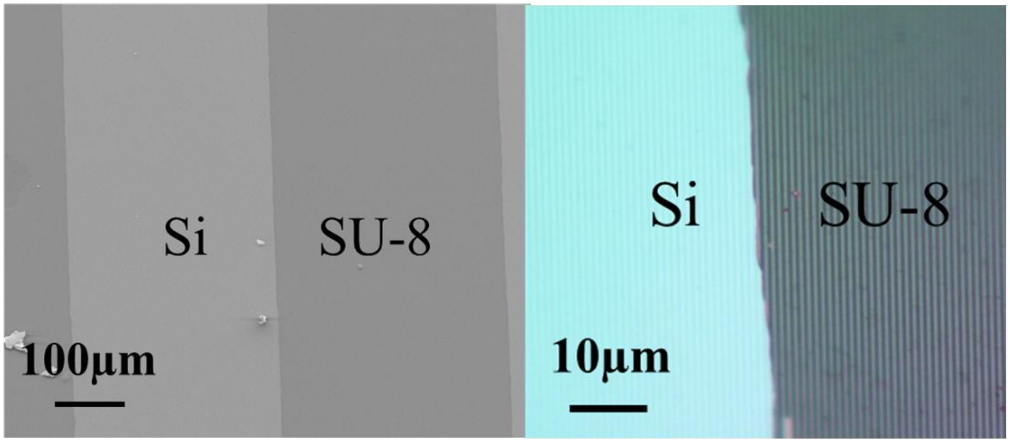


Figure 27. SEM Image of SU-8/Si Junction (a) and Optical Image of the Gratings Written on SU-8/Si Junction Using EBL (b).

We should point out that this silicon surface is coming from the unpolished side of the device layer and is relatively rough compared to the polished silicon surface. As a result the rough surface can abate the reflection of the laser light. Also, the sidewalls of the silicon strips are relatively deep (>10 µm) and therefore are neither vertical nor perfectly smooth due to isotropic dry etching. After filling with the SU-8 and baking it is possible that cracks or delamination at the interface of the sidewalls are present due to the large CTE mismatch between SU-8 and Si.

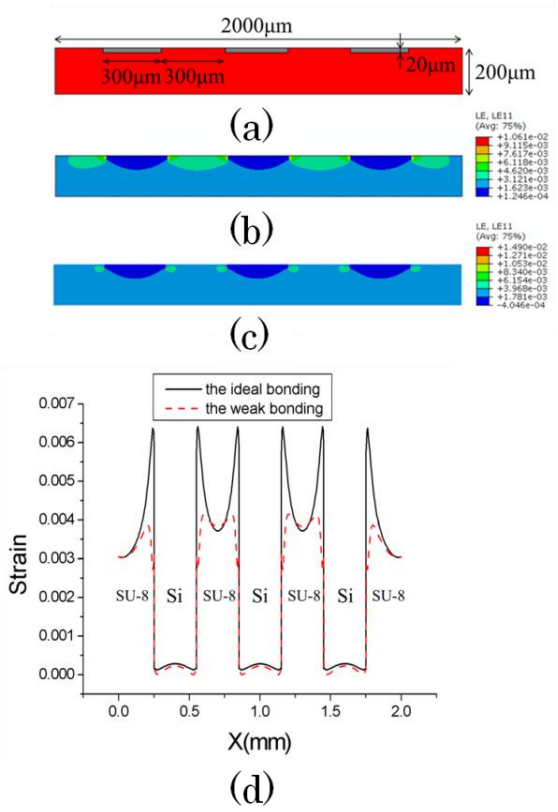


Figure 28. (a) Schematic of the SU-8/Si Junction Structure. (b) Strain Contours in the Horizontal Direction on the Surface for the Ideal Bonding Case and (c) for the Weak Bonding Case. (d) Strain as a Function of the Horizontal Distance on the Top Surface of Structure. Here the Temperature Change $\Delta T$ is 45˚C.

The commercial finite element package ABAQUS is used to simulate the thermal deformation of the junction structure of SU-8/Si when subjected to temperature changes. Fig. 28(a) shows the model, including three 300-μm-width by 20-μm-thick silicon strips embedded in a 200-μm-thick by 2000-μm-long SU-8 substrate with 300 μm spacing between the strips. The thermal strain analysis is conducted by introducing a uniform temperature change $\Delta T$ in the whole domain. The silicon and SU-8 are modeled by a 4-

node bilinear plane strain element (CPE4) for two different cases. In case one, the ideal bonding, the SU-8/Si interface is treated as shared nodes which indicates that there is perfect bonding between the silicon strips and the SU-8 substrate on both the bottom and the two sides. In the latter case, the weak bonding case, the silicon strips are connected to the SU-8 substrate only through the bottom using TIE constraint and there is no bonding with the SU-8 on the two sides of each silicon strip. The weak bonding case is used to simulate a scenario when the bonding is less than ideal and there is delamination on the two sides. The following material parameters are used in the analysis: $E_{SU-8}$ = 2 GPa, $v_{SU-8}$ = 0.3, $\alpha_{SU-8}$ = 52 × 10-6 /˚C, $E_{Si}$ = 130 GPa, $v_{Si}$ = 0.3, $\alpha_{Si}$ = 2.6 × 10-6 /˚C, $\Delta T$ = 45˚C, where $E$, $v$ and $\alpha$ are Young's modulus, Poisson's ratio and the CTE, respectively. We assume that the surface is ideally flat and there is no existent warping conditions.

Strain contours in the horizontal direction on the top surface of the structure are shown in Fig. 28(b) for the ideal bonding case and (c) for the weak bonding case. Fig. 28(d) shows the strain as a function of horizontal distance on the top surface of the junction structure for the two cases. The strain on the SU-8 area is much higher than that of the silicon strips and when subject to a temperature change of 45 ˚C, the junction experiences a sudden strain change due to the CTE mismatch. The strain on the silicon surface fluctuate slightly and the two ranges are at the same level for both cases: $1.3 \times 10^{-4}$~$2.9 \times 10^{-4}$ for the ideal bonding case and $8 \times 10^{-6}$~$2.3 \times 10^{-4}$ for the weak bonding case. But the strain ranges differ greatly on the surface of SU-8, ranging from $3.7 \times 10^{-3}$ to $6.4 \times 10^{-3}$ while exhibiting very sharp peaks for the ideal bonding case. However, in the weak bonding case, the strain ranges from $3.8 \times 10^{-3}$ to $4.1 \times 10^{-3}$ while exhibiting blunt peaks This is reasonable since the surface of the SU-8 pattern has more constraints on the two

sides from the silicon strips while under thermo-mechanical loading, and therefore has a steeper strain gradient across the SU-8 surface along with a sharp strain jump on the edges for the ideal bonding case.

Electronic packages are typically integrated with various different materials with a mismatched CTE, which leads to a complicated distribution of strain across the whole package. To evaluate the applicability of this laser scanning technique for strain mapping, we tested a composite sample as described in the preceding section to model a simplified case of strain distribution. The results were compared with thermal strain distributions calculated by FEA for a similar sample structure. The comparison between the measurement and simulation results evaluates the feasibility of applying this laser scanning technique towards advanced applications of electronic packages.

We first fabricated a uniform grating structure with an 800 nm wavelength across consecutive SU-8/Si strip samples using EBL and metal lift-off techniques. Ideally, for a uniform material, the grating wavelength will not change across the sample. After heating the composite sample made of CTE mismatched materials, such as SU-8/Si strips as we fabricated and discussed above, the sample will experience unevenly distributed thermal strain depending on the thermal expansion from the underlying substrates and the constraints from the surrounding materials. By measuring the degree of expansion at the surface, one can map the strain distribution on the composite sample. The grating pattern fabricated onto the composite sample contracts and expands to follow the expansion of the underlying substrate, and thus, records the strain information. By spatially scanning the sample with a small laser spot size, the grating wavelength variation is captured by the camera as a shift in the diffraction peak position, which can be translated back into

strain information through data processing. Thus the SU-8/Si composite samples that were fabricated with a grating were tested to validate the capability of this strain sensing technique.

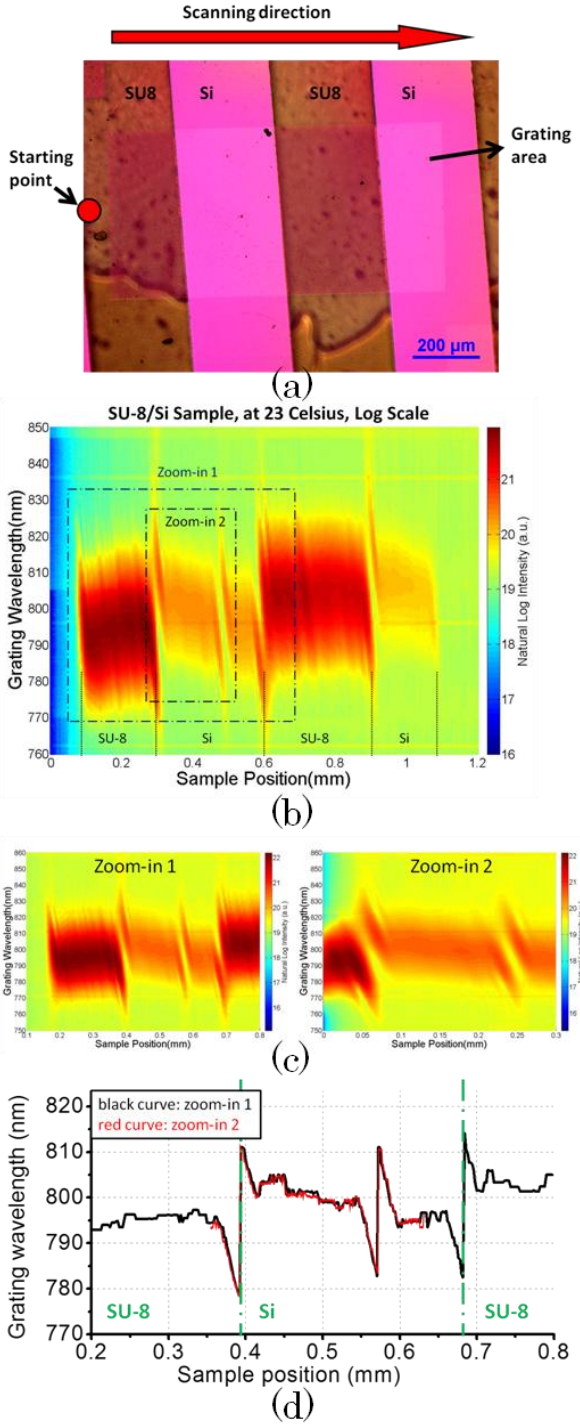

Figure 29. (a) Optical Image of the Grating Area on the SU-8/Si Substrate, Marked with the Scanning Area and Direction. (b) Contour Plot of the 1D Scan Across the SU-8/Si Composite Structure, Using a Linear Scale. (c) Contour Plots with Smaller Sample Scanning Step Size, 2 μm (left) and 1μm (right), for the Highlighted Region in (b). (d) Superimposed Plots of the Extracted Grating Wavelength versus Sample Position from Contour Plots in (c).

Figure 29(a) shows the optical image of one grating pattern fabricated onto the SU-8/Si composite sample. The whole grating pattern covers an area of 1 mm by 0.5 mm. As observed from the optical image, the grating lines are not perfectly aligned with the SU-8/Si strips, which affects the captured diffraction light signal when the laser is shining on the interface of the two different strips. Observing the high magnification optical image of the grating area confirms that the grating quality of the Si strips is not as good as the grating on the SU-8 strips. This is likely caused by the EBL lithography process that involves developing and lift-off in solutions that can distort the 300 μm thick SU-8 sample. The other direct observation from the optical image is that the whole SU-8/Si composite sample is not flat after fabrication with the EBL defined grating pattern, which can be the result of a non-flat surface from the epoxy that was used to attach the thin sample to the sample stage. In addition, the sample exhibits warping due to the thermal heating and immersion in acetone during the fabrication process of making the gold grating patterns. Therefore even at room temperature, the grating wavelength does not appear to be at a constant 800 nm across the entire pattern, even though the original intention was to design a uniform grating pattern. This can be seen in the contour plots

for measurement results in Fig. 29. However, this non-uniform strain observed from the sample illustrates the power of this laser scanning technique which can delineate strain variation at a very high spatial resolution.

The laser beam was scanned across the entire grating region by increments of 5 μm, as demonstrated in Fig. 29(a) with the scanning area and scanning direction at room temperature (23˚C). The testing results are depicted on the contour plot in Fig. 29(b). The diffraction light intensity from the SU-8 substrate is indeed stronger than the signal from the Si substrate, which is likely due to the wavering quality of grating patterns on those regions: the SU-8 surface is smoother than the unpolished side of the Si surface from the original SOI wafer. At room temperature, the extracted grating wavelength already appears to show small amounts of variances versus the laser spot position. The information recorded from the room temperature scan is a combination of factors that alter the diffraction angle from the grating pattern. Some of the factors can be explained, while others cannot be fully interpreted using the current system setup.

In order to verify the repeatability of the recorded grating wavelength variation, two additional 1D scans with smaller step sizes were conducted at the same temperature, which also shows more detailed information. Both scans displayed in Fig. 29(c), cover the Si region where there is a discontinuity in the grating pattern which comes from a noticeable imperfection in the grating pattern. By superimposing the extracted grating wavelength versus sample position plots from the two zoom-in scans, one observes that the three small steps within the silicon region repeats itself in those two independent measurements. The height of the steps is also about 2~4 nm, which confirms that it is a signal coming from the sample instead of random noise. Note that the previous CTE

extraction of silicon sample validates that even 10 micro-strain is detectable from this laser scanning technique. The dimension of the steps is between 20-30 μm. This indicates that the resolvable feature size from the laser scanning technique is at least 20 μm, thus demonstrating the spatial resolution. One strategy to improve the spatial resolution is to further reduce the laser spot size. Hence, with a sufficient number of sample steps and fine step sizes along with a proper laser spot size, one should be able to compose a comprehensive and accurate strain map.

The same pattern has been scanned at an elevated temperature of 68˚C to examine the thermal strain and its spatial variation. The results are plotted in Fig. 30(a) as a contour plot. The diffraction signal shifts up, which indicates that the grating periodicity increases as a result of thermal expansion. The whole pattern exhibits a lateral shift as well, which is caused by the thermal drift in the sample. Quantitative comparison is performed by superimposing the plots of the extracted grating wavelength versus sample position under two different temperatures, which can be seen in Fig. 30(b). The SU-8 region expands more under thermal loading than the Si regions, which is consistent with the simulation predictions. Something interesting is that the width of the heated up pattern is wider than the width of the pattern before heating. Therefore, compensations have been applied for the calculation of the grating wavelength difference, but are not displayed in the grating wavelength versus sample position plot in Fig. 30(b). The strain distributions within the highlighted regions are plotted. From left to right on the SU-8 strip, the strain varies between $6 \times 10^{-3}$ and $3 \times 10^{-3}$. On the Si strip, the strain variation is between $6 \times 10^{-4}$ and $1 \times 10^{-3}$. The experimental results from SU-8 region are slightly smaller than the FEA predictions while the experimental results from Si region are larger

than the finite element simulations. However, comparing the experimental results between the different regions matches the simulation work.

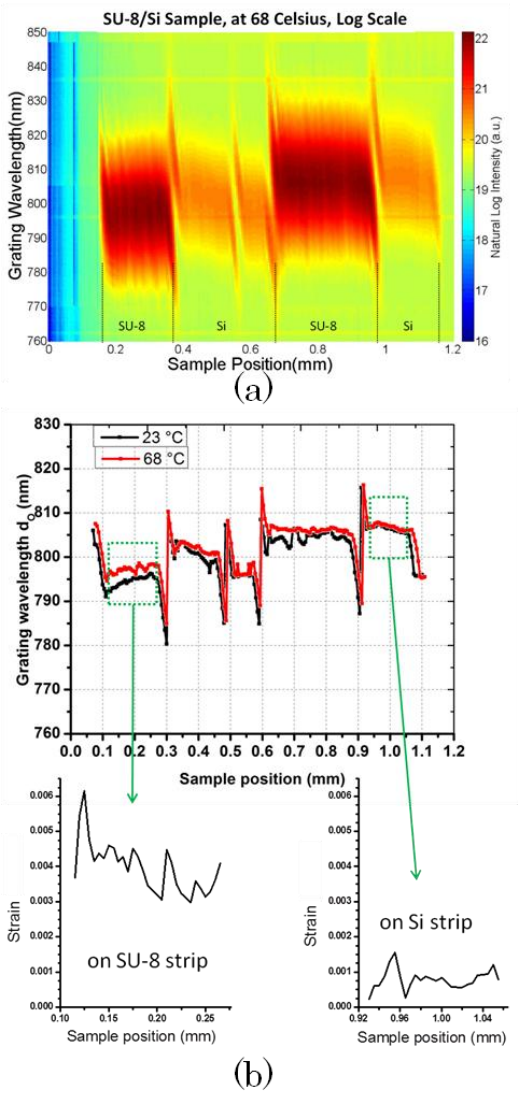


Figure 30. Contour Plot of SU-8/Si Composite Sample at 68˚C is Presented in (a). The Corresponding Extracted Grating Wavelength is Plotted as Red Curve in (b), while the Extracted Grating Wavelength at 23˚C (Fig. 29(b)) is Plotted as the Black Curve. Strain is Calculated for SU-8 and Si Regions, Based on the Difference between the Two Temperatures.

Strain distribution analysis isn't done on the middle region. This is because the strain information in these regions is dominated by other effects, such as warping and imperfections on the grating patterns. Although these factors may impact the regions where analysis is done, they are minor effects compared to the effects discussed in the FEA work.

## 6.4 Strain Mapping on Microelectronic Packages

In this work, the laser scanning technique has been applied to map the two dimensional strain distribution on the microelectronic package sample. The sample is cut to expose the cross-section of the die-interconnect-substrate region, and fine polished to make the cross-section surface smooth. One of the regions of interest (ROI) is the solder bump region, as shown in Fig. 31, where a solder bump, connecting copper wires at top and bottom, is surrounded by epoxy. The dissimilar materials in this region will result in different thermal expansion rates according to their different CTEs. Hence an uneven strain distribution will be induced into the sample when the sample subjects to the elevated temperature. The solder bumps have a width of around 60-80 μm, while the spacing between the neighboring solder bumps is about 120 μm. The previous spatial resolution study successfully resolved the similar pattern, the multiple 50 μm domain pattern. Therefore the ROI 1 is a good starting point for calibration with modeling and other metrology. As circled in Fig. 31(a), the grating patterns will be placed at the corners in order to map the highest thermal strain experienced by the sample.

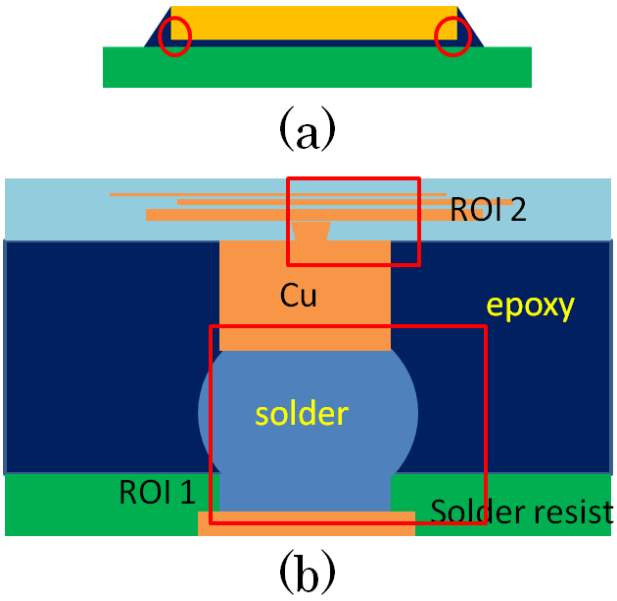


Figure 31. (a) Target Areas around First 1~2 Bumps from Both Sides for Highest Stress (or Maximum Signal). (b) ROI 1: Solder Region. Large Deformation Can Be Observed and Measured. Easy to Calibrate with Modeling and Other Metrology. ROI 2: Metal Line Region in Si. True ROI to Demonstrate the Value of this Metrology. A Different Grating Size Might Be Needed.

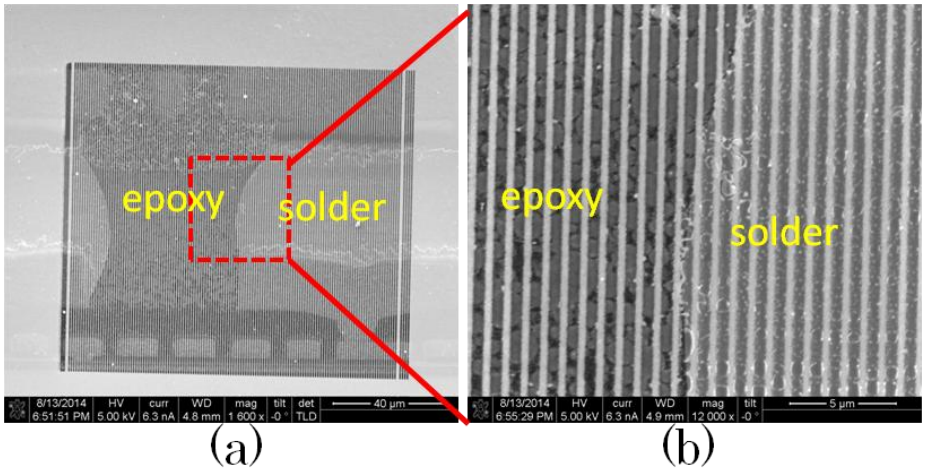


Figure 32. SEM Images of Gratings on Microelectronic Package's Cross-Section. (b) The Zoom-in Image of the Highlighted Region in (a).

Grating lines are written on the ROI 1 using focused ion beam (FIB), with a pattern size of 120 μm by 120 μm. The grating lines will follow the expansion of the underneath substrate freely, in order to play a role as the strain sensor. Two dimensional scans are performed across the sample, at room temperature and at an elevated temperature of 116˚C. The detailed scanning conditions are listed as following. Vertical scan step size: 5 μm. Horizontal scan step size: 3 μm with 50 steps. Scan direction: from left to right; from top to bottom, within the green box marked in Fig.33. Temperature: 24˚C and 116˚C. The diffraction signal is recorded at each sample position, and is later applied to the calculation of the grating wavelength variation, which directly reflects the thermal expansion for the substrate.

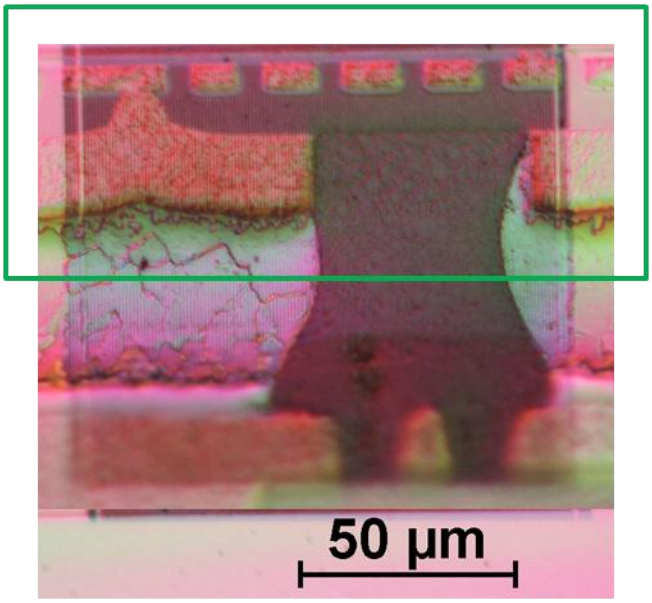


Figure 33. Optical Image of the Interested Solder Bump Region Covered with FIB Scribed Grating Lines. The Scanned Region is Highlighted in the Green Box.

Figure 34 and 35 display the sets of 1D scan results at different vertical sample positions for each temperature.

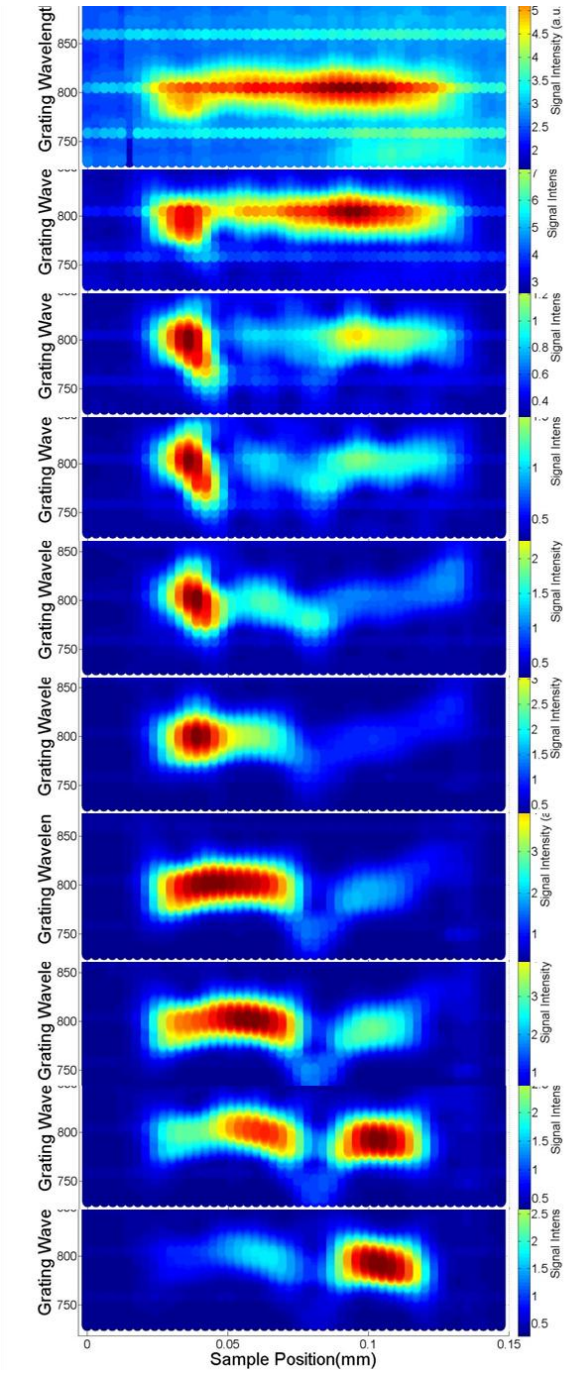


Figure 34. 1D Scans across the Region Marked in Fig. 33 with a Series of Vertical Steps, at 24℃.

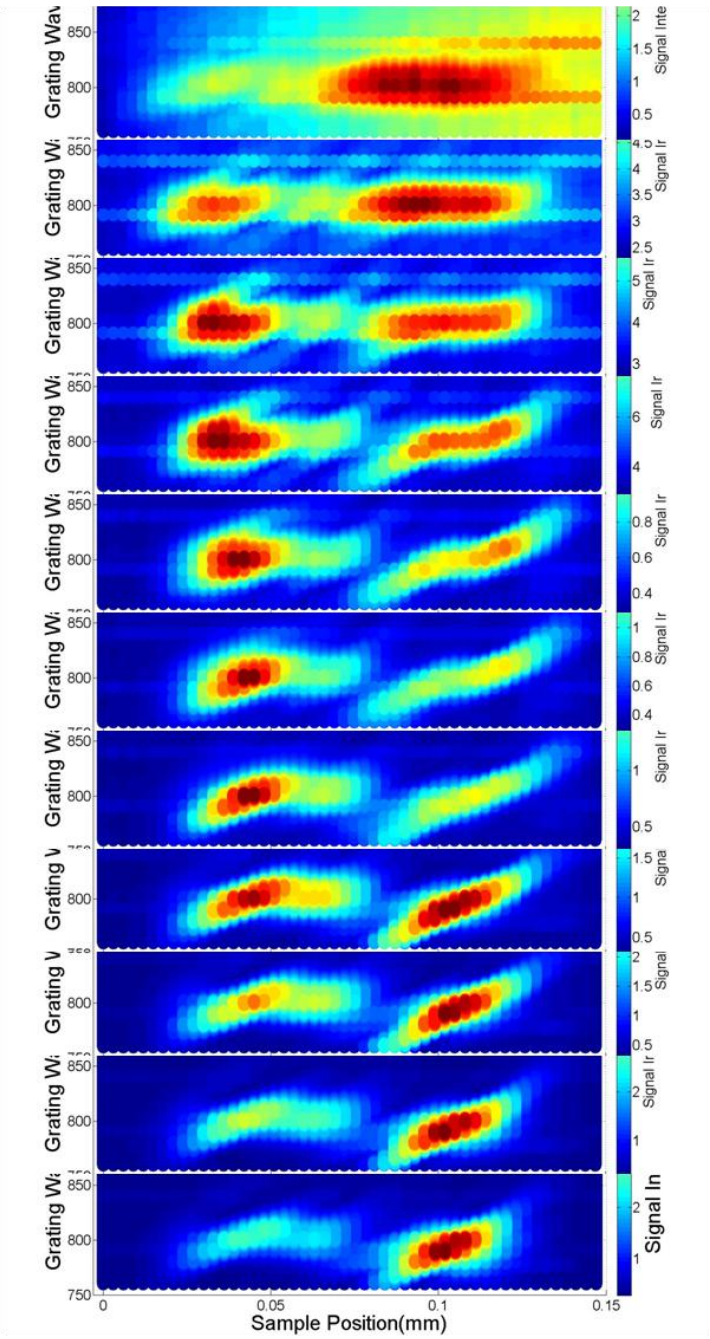


Figure 35. 1D Scans across the Region Marked in Fig. 33 with a Series of Vertical Steps, at 116℃.

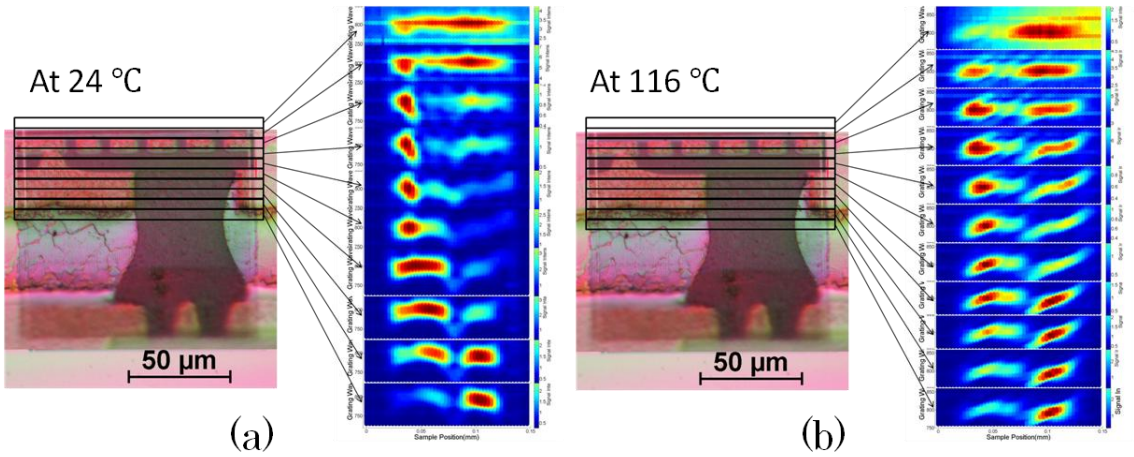


Figure 36. 2D Scan Results at Two Temperatures as Labeled, also with Marked Scan Region for Each Vertical Position.

The two sets of 1D scan results in Fig. 34 and Fig. 35 are displayed side by side in Fig. 36, in which each 1D contour plot is corresponded to the scan area on the interested solder bump region. Even at room temperature, the FIB scribed grating pattern is not uniform. Since FIB uses a high energy ion beam to write the grating pattern, it induces local heat into the substrate, and thus the grating lines exhibits the strain from the ion beam according to the local thermal expansion rate. At a high temperature, the scan across the same sample area results in similar patterns. The difference comes from the uneven expansion within the area. There is an ongoing effort to develop the data processing program to quantitatively analyze the 2D strain map, especially for direct extraction of the strain information from 2D contour plots, as shown in Fig. 37.

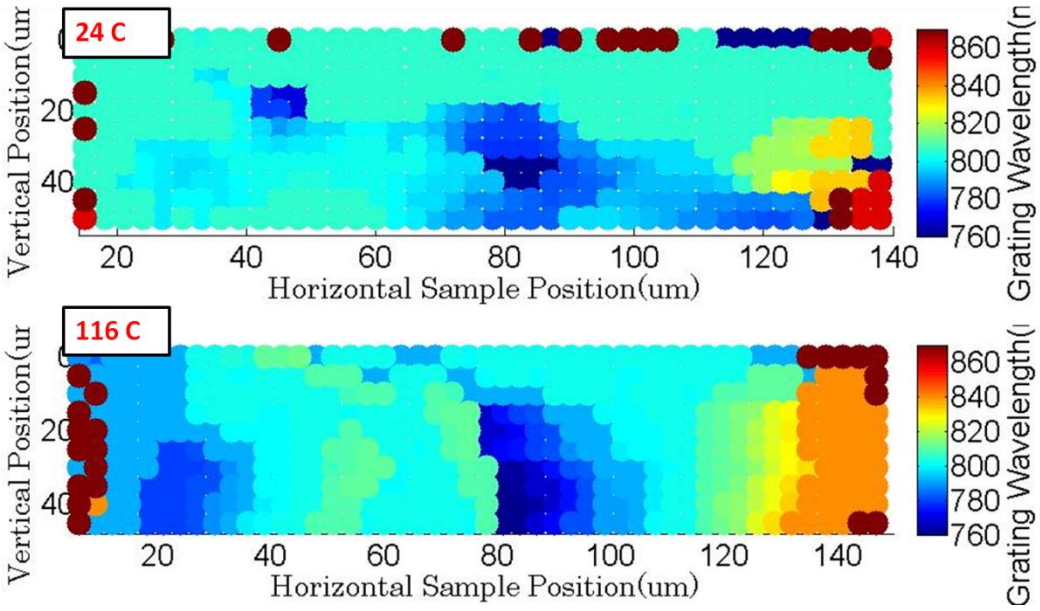


Figure 37. Contour Plots of the 2D Mapping Results on the Scanned Region Shown in Fig. 33, at 24℃ and 116℃.

# CHAPTER 7

## Conclusion

The laser scanning technique is demonstrated to have both high strain sensitivity and high spatial resolution on pre-defined samples. Note that this technique is capable of detecting localized strain, unlike Moiré techniques (which relies on a sufficient field of view to form the Moiré pattern). The CTE measurement for silicon proves that the detectable strain to be as small as 0.00001. Even though the entire elevated temperature range is only 30˚C, it indicates the capability for monitoring small CTE materials such as Si. This has many applications in different packaging processes, such as reflow, which typically occurs at over 200˚C. Scanning the EBL defined pattern validates the resolvable feature size to be as small as 10 μm. This technique in principle, is able to scan an unlimited field of view, which is determined by the traveling distance of the translational stage. The investigation of strain distribution on the composite sample under thermal loading validates the feasibility of applying this technique towards electronic packages. 2D scanning has been applied to the interested solder bump region in microelectronic package. The quantitative analysis for the accurate strain information exaction from the 2D contour plots is under development.

Comparing to micro Moiré and SEM DIC, this strain sensing technique can provide large field of view for large area strain mapping applications. The fabricated zero-thickness gratings during this project can also be utilized in micro Moiré and SEM DIC measurements. However, the zero-thickness gratings fabricated using soft contact lithography and FIB are not ideal in terms of uniformity, which adds complexity to the Moiré pattern. For this strain sensing technique, an initial scan is performed to generate

the reference strain map. The strain information is then extracted by deducting the reference from the strain maps with strain loading, where the initial grating patterns are not necessary to be ideally uniform.

Future work of the project includes the following parts.

Firstly, it is necessary to improve the imaging system for monitoring the laser spot position onto the target sample surface. Therefore, it is necessary to design an improved illumination system, incorporate a better imaging camera, and utilize the auto-focus ability (optional). If it is not applicable for adding an auto-focus system, an alternative way is to do independent calibration of diffraction angle versus peak position at different temperatures.

Secondly, more electronic package samples fabricated with FIB gratings are needed, in order to test out the optimized grating patterns for the measurement.

Last but not the least, upgraded software with new functionalities. It is necessary to add more functionalities to the LabVIEW GUI to instantly display the measurement results so that it can directly give feedback to help with setup adjustment.

REFERENCES


[1] F. Garnier, R. Hajlaoui, A. Yassar, and P. Srivastava, "ALL-POLYMER FIELD-EFFECT TRANSISTOR REALIZED BY PRINTING TECHNIQUES," *Science,* vol. 265, pp. 1684-1686, Sep 1994.

[2] J. A. Rogers, Z. Bao, K. Baldwin, A. Dodabalapur, B. Crone, V. R. Raju, *et al.*, "Paper-like electronic displays: Large-area rubber-stamped plastic sheets of electronics and microencapsulated electrophoretic inks," *Proceedings of the National Academy of Sciences of the United States of America,* vol. 98, pp. 4835-4840, Apr 2001.

[3] X. F. Duan, C. M. Niu, V. Sahi, J. Chen, J. W. Parce, S. Empedocles, *et al.*, "High-performance thin-film transistors using semiconductor nanowires and nanoribbons," *Nature,* vol. 425, pp. 274-278, Sep 2003.

[4] S. R. Forrest, "The path to ubiquitous and low-cost organic electronic appliances on plastic," *Nature,* vol. 428, pp. 911-918, Apr 2004.

[5] K. Nomura, H. Ohta, A. Takagi, T. Kamiya, M. Hirano, and H. Hosono, "Room-temperature fabrication of transparent flexible thin-film transistors using amorphous oxide semiconductors," *Nature,* vol. 432, pp. 488-492, Nov 2004.

[6] S. Bae, H. Kim, Y. Lee, X. F. Xu, J. S. Park, Y. Zheng, *et al.*, "Roll-to-roll production of 30-inch graphene films for transparent electrodes," *Nature Nanotechnology,* vol. 5, pp. 574-578, Aug 2010.

[7] H. Gao, R. Tang, T. Ma, H. Jiang, H. Yu, and G. J. Cheng, "Laser Shock-Induced Conformal Transferring of Functional Devices on 3-D Stretchable Substrates," *Microelectromechanical Systems, Journal of,* vol. PP, pp. 1-1, 2014.

[8] F. Yu, J. Lee, N. Jen, X. Li, Q. Zhang, R. Tang, *et al.*, "Elevated electrochemical impedance in the endoluminal regions with high shear stress: Implication for assessing lipid-rich atherosclerotic lesions," *Biosensors and Bioelectronics,* vol. 43, pp. 237-244, 5/15/ 2013.

[9] T. Rui, H. Hai, Y. Yong Mo, J. Oiler, L. Mengbing, and Y. Hongyu, "Three-Dimensional Flexible Thermal Sensor for Intravascular Flow Monitoring," *Sensors Journal, IEEE,* vol. 13, pp. 3991-3998, 2013.

[10] G. Huang, T. Rui, M. Teng, J. Hanqing, Y. Hongyu, and G. J. Cheng, "Direct Integration of Functional Structures on 3-D Microscale Surfaces by Laser Dynamic Forming," *Microelectromechanical Systems, Journal of,* vol. 22, pp. 1428-1437, 2013.

[11] R. Tang, H. Huang, H. E. Tu, H. S. Liang, M. B. Liang, Z. M. Song, *et al.*, "Origami-enabled deformable silicon solar cells," *Applied Physics Letters,* vol. 104, Feb 2014.

[12] Z. Suo, E. Y. Ma, H. Gleskova, and S. Wagner, "Mechanics of rollable and foldable film-on-foil electronics," *Applied Physics Letters,* vol. 74, pp. 1177-1179, Feb 1999.

[13] D. H. Kim, J. H. Ahn, W. M. Choi, H. S. Kim, T. H. Kim, J. Z. Song, *et al.*, "Stretchable and foldable silicon integrated circuits," *Science,* vol. 320, pp. 507-511, Apr 2008.

[14] A. C. Siegel, S. T. Phillips, M. D. Dickey, N. S. Lu, Z. G. Suo, and G. M. Whitesides, "Foldable Printed Circuit Boards on Paper Substrates," *Advanced Functional Materials,* vol. 20, pp. 28-35, Jan 2010.

[15] C. Yang, H. W. Gu, W. Lin, M. M. Yuen, C. P. Wong, M. Y. Xiong, *et al.*, "Silver Nanowires: From Scalable Synthesis to Recyclable Foldable Electronics," *Advanced Materials,* vol. 23, pp. 3052-+, Jul 2011.

[16] H. G. Tu, H. Q. Jiang, H. Y. Yu, and Y. Xu, "Hybrid silicon-polymer platform for self-locking and self-deploying origami," *Applied Physics Letters,* vol. 103, Dec 2013.

[17] S. M. Hayes, N. Chawla, and D. R. Frear, "Interfacial fracture toughness of Pb-free solders," *Microelectronics Reliability,* vol. 49, pp. 269-287, Mar 2009.

[18] Y. J. Wen and C. Basaran, "An analytical model for thermal stress analysis of multi-layered microelectronic packaging," *Mechanics of Materials,* vol. 36, pp. 369-385, Apr 2004.

[19] Q. Yu and M. Shiratori, "Fatigue-strength prediction of microelectronics solder joints under thermal cyclic loading," *Ieee Transactions on Components*

*Packaging and Manufacturing Technology Part A*, vol. 20, pp. 266-273, Sep 1997.

[20] X. Y. He, D. Q. Zou, and S. Liu, "Phase-shifting analysis in moire interferometry and its applications in electronic packaging," *Optical Engineering,* vol. 37, pp. 1410-1419, May 1998.

[21] H. M. Xie, H. X. Shang, F. L. Dai, B. Li, and Y. M. Xing, "Phase shifting SEM moire method," *Optics and Laser Technology*, vol. 36, pp. 291-297, Jun 2004.

[22] F. Lagattu, F. Bridier, P. Villechalse, and J. Brillaud, "In-plane strain measurements on a microscopic scale by coupling digital image correlation and an in situ SEM technique," *Materials Characterization,* vol. 56, pp. 10-18, Jan 2006.

[23] P. G. Ifju and B. Han, "Recent Applications of Moire Interferometry," *Experimental Mechanics,* vol. 50, pp. 1129-1147, Oct 2010.

[24] D. Nowell, R. J. H. Paynter, and P. F. P. De Matos, "Optical methods for measurement of fatigue crack closure: moire interferometry and digital image correlation," *Fatigue & Fracture of Engineering Materials & Structures,* vol. 33, pp. 778-790, Dec 2010.

[25] M. J. Tang, H. M. Xie, J. G. Zhu, X. J. Li, and Y. J. Li, "Study of moire grating fabrication on metal samples using nanoimprint lithography," *Optics Express,* vol. 20, pp. 2942-2955, Jan 2012.

[26] B. Pan, K. Qian, H. Xie, and A. Asundi, "Two-dimensional digital image correlation for in-plane displacement and strain measurement: a review," *Measurement Science & Technology,* vol. 20, Jun 2009.

[27] G. Vendroux and W. G. Knauss, "Submicron deformation field measurements: Part 2. Improved digital image correlation," *Experimental Mechanics,* vol. 38, pp. 86-92, Jun 1998.

[28] E. Verhulp, B. van Rietbergen, and R. Huiskes, "A three-dimensional digital image correlation technique for strain measurements in microstructures," *Journal of Biomechanics,* vol. 37, pp. 1313-1320, Sep 2004.

[29] P. Zhou and K. E. Goodson, "Subpixel displacement and deformation gradient measurement using digital image/speckle correlation (DISC)," *Optical Engineering,* vol. 40, pp. 1613-1620, Aug 2001.

[30] H. Lu and P. D. Cary, "Deformation measurements by digital image correlation: Implementation of a second-order displacement gradient," *Experimental Mechanics,* vol. 40, pp. 393-400, Dec 2000.

[31] B. Winiarski, G. S. Schajer, and P. J. Withers, "Surface Decoration for Improving the Accuracy of Displacement Measurements by Digital Image Correlation in SEM," *Experimental Mechanics,* vol. 52, pp. 793-804, Sep 2012.

[32] Z. B. Zhou, P. W. Chen, F. L. Huang, and S. Q. Liu, "Experimental study on the micromechanical behavior of a PBX simulant using SEM and digital image correlation method," *Optics and Lasers in Engineering,* vol. 49, pp. 366-370, Mar 2011.

[33] M. A. Sutton, N. Li, D. C. Joy, A. P. Reynolds, and X. Li, "Scanning electron microscopy for quantitative small and large deformation measurements part i: SEM imaging at magnifications from 200 to 10,000," *Experimental Mechanics,* vol. 47, pp. 775-787, Dec 2007.

[34] M. A. Sutton, N. Li, D. Garcia, N. Cornille, J. J. Orteu, S. R. McNeill, *et al.*, "Scanning electron microscopy for quantitative small and large deformation measurements - part II: Experimental validation for magnifications from 200 to 10,000," *Experimental Mechanics,* vol. 47, pp. 789-804, Dec 2007.

[35] K. T. Huang and H. C. Chen, "Automatic Measurement and Stress Analysis of ITO/PET Flexible Substrate by Shadow Moire Interferometer With Phase-Shifting Interferometry," *Journal of Display Technology,* vol. 10, pp. 609-614, Jul 2014.

[36] H. B. Du, J. H. Wang, H. Zhao, and P. P. Jia, "Calibration of the high sensitivity shadow moire system using random phase-shifting technique," *Optics and Lasers in Engineering,* vol. 63, pp. 70-75, Dec 2014.

[37] H. B. Du, J. H. Wang, H. Zhao, F. F. Gu, and J. L. Zhao, "Phase extraction from random phase-shifted shadow moire fringe patterns using stereovision technique," *Optical Engineering,* vol. 53, Apr 2014.

[38] J. Degrieck, W. Van Paepegem, and P. Boone, "Application of digital phase-shift shadow Moire to micro deformation measurements of curved surfaces," *Optics and Lasers in Engineering,* vol. 36, pp. 29-40, Jul 2001.

[39] J. M. Huntley, "Automated fringe pattern analysis in experimental mechanics: a review," *Journal of Strain Analysis for Engineering Design,* vol. 33, pp. 105-125, Mar 1998.

[40] G. Mauvoisin, F. Bremand, and A. Lagarde, "3-DIMENSIONAL SHAPE RECONSTRUCTION BY PHASE-SHIFTING SHADOW MOIRE," *Applied Optics,* vol. 33, pp. 2163-2169, Apr 1994.

[41] T. Yoshizawa and T. Tomisawa, "SHADOW MOIRE TOPOGRAPHY BY MEANS OF THE PHASE-SHIFT METHOD," *Optical Engineering,* vol. 32, pp. 1668-1674, Jul 1993.

[42] M. A. Sutton, J. H. Yan, V. Tiwari, H. W. Schreier, and J. J. Orteu, "The effect of out-of-plane motion on 2D and 3D digital image correlation measurements," *Optics and Lasers in Engineering,* vol. 46, pp. 746-757, Oct 2008.

[43] M. A. Sutton, X. Ke, S. M. Lessner, M. Goldbach, M. Yost, F. Zhao, *et al.*, "Strain field measurements on mouse carotid arteries using microscopic three-dimensional digital image correlation," *Journal of Biomedical Materials Research Part A,* vol. 84A, pp. 178-190, Jan 2008.

[44] T. A. Berfield, J. K. Patel, R. G. Shimmin, P. V. Braun, J. Lambros, and N. R. Sottos, "Micro- and nanoscale deformation measurement of surface and internal planes via digital image correlation," *Experimental Mechanics,* vol. 47, pp. 51-62, Feb 2007.

[45] Z. L. Sun, J. S. Lyons, and S. R. McNeill, "Measuring microscopic deformations with digital image correlation," *Optics and Lasers in Engineering,* vol. 27, pp. 409-428, Jul 1997.

[46] Y. M. He, Y. Sun, J. Zhang, and X. D. Li, "An analysis of deformation mechanism in the Si3N4-AgCuTi + SiCp-Si3N4 joints by digital image correlation," *Journal of the European Ceramic Society,* vol. 33, pp. 157-164, Jan 2013.

[47] S. Y. Yang, I. Kim, and S. B. Lee, "A study on the thermal fatigue behavior of solder joints under power cycling conditions," *Ieee Transactions on Components and Packaging Technologies,* vol. 31, pp. 3-12, Mar 2008.

[48] H. Ghadbeigi, C. Pinna, S. Celotto, and J. R. Yates, "Local plastic strain evolution in a high strength dual-phase steel," *Materials Science and Engineering a-Structural Materials Properties Microstructure and Processing,* vol. 527, pp. 5026-5032, Jul 2010.

[49] N. Sabate, D. Vogel, A. Gollhardt, J. Marcos, I. Gracia, C. Cane, *et al.*, "Digital image correlation of nanoscale deformation fields for local stress measurement in thin films," *Nanotechnology,* vol. 17, pp. 5264-5270, Oct 2006.

[50] W. D. Lockwood and A. P. Reynolds, "Use and verification of digital image correlation for automated 3-D surface characterization in the scanning electron microscope," *Materials Characterization,* vol. 42, pp. 123-134, Feb-Mar 1999.

[51] J. Kang, M. Jain, D. S. Wilkinson, and J. D. Embury, "Microscopic strain mapping using scanning electron microscopy topography image correlation at large strain," *Journal of Strain Analysis for Engineering Design,* vol. 40, pp. 559-570, Aug 2005.

[52] H. Jin, W. Y. Lu, and J. Korellis, "Micro-scale deformation measurement using the digital image correlation technique and scanning electron microscope imaging," *Journal of Strain Analysis for Engineering Design,* vol. 43, pp. 719-728, Nov 2008.

[53] N. Li, M. A. Sutton, X. Li, and H. W. Schreier, "Full-field thermal deformation measurements in a scanning electron microscope by 2D digital image correlation," *Experimental Mechanics,* vol. 48, pp. 635-646, Oct 2008.

[54] Z. H. Xu, X. D. Li, M. A. Sutton, and N. Li, "Drift and spatial distortion elimination in atomic force microscopy images by the digital image correlation technique," *Journal of Strain Analysis for Engineering Design,* vol. 43, pp. 729-743, Nov 2008.

[55] A. M. Korsunsky, M. Sebastiani, and E. Bemporad, "Residual stress evaluation at the micrometer scale: Analysis of thin coatings by FIB milling and digital image correlation," *Surface & Coatings Technology,* vol. 205, pp. 2393-2403, Dec 2010.

[56] J. W. Joo and S. H. Choa, "Deformation behavior of MEMS gyroscope sensor package subjected to temperature change," *Ieee Transactions on Components and Packaging Technologies*, vol. 30, pp. 346-354, Jun 2007.

[57] K. Han, M. Ciccotti, and S. Roux, "Measuring nanoscale stress intensity factors with an atomic force microscope," *Epl*, vol. 89, Mar 2010.

[58] Y. F. Sun and J. H. L. Pang, "AFM image reconstruction for deformation measurements by digital image correlation," *Nanotechnology*, vol. 17, pp. 933-939, Feb 2006.

[59] Y. F. Sun, J. H. L. Pang, and W. Fan, "Nanoscale deformation measurement of microscale interconnection assemblies by a digital image correlation technique," *Nanotechnology*, vol. 18, Oct 2007.

[60] J. C. Chen, Y. D. Yan, T. Sun, Y. Qi, and X. D. Li, "Probing the Roles of Polymeric Separators in Lithium-Ion Battery Capacity Fade at Elevated Temperatures," *Journal of the Electrochemical Society*, vol. 161, pp. A1241-A1246, 2014.

[61] Y. Wang, T. Ma, H. Yu, and H. Jiang, "Random analysis on controlled buckling structure for energy harvesting," *Applied Physics Letters*, vol. 102, p. 041915, 2013.

[62] T. Ma, H. Liang, G. Chen, B. Poon, H. Jiang, and H. Yu, "Micro-strain sensing using wrinkled stiff thin films on soft substrates as tunable optical grating," *Optics express*, vol. 21, pp. 11994-12001, 2013.

[63] P. Chatterjee, Y. Pan, E. C. Stevens, T. Ma, H. Jiang, and L. L. Dai, "Controlled Morphology of Thin Film Silicon Integrated with Environmentally Responsive Hydrogels," *Langmuir*, vol. 29, pp. 6495-6501, 2013.

[64] T. Ma, Y. Wang, R. Tang, H. Yu, and H. Jiang, "Pre-patterned ZnO nanoribbons on soft substrates for stretchable energy harvesting applications," *Journal of Applied Physics*, vol. 113, p. 204503, 2013.

[65] C. Yu, Y. Pan, H. Ma, T. Ma, J. Zhang, Y. Song, *et al.*, "Thermoresponsiveness of Integrated Ultra‐Thin Silicon with Poly (N‐isopropylacrylamide) Hydrogels," *Macromolecular rapid communications*, vol. 32, pp. 820-824, 2011.

[66] H. C. Hong and C. M. Chen, "Design, Fabrication and Failure Analysis of Stretchable Electrical Routings," *Sensors,* vol. 14, pp. 11855-11877, Jul 2014.

[67] Y. H. Yun, S. A. Jang, and Y. J. Oh, "Formation of Stretchable Metal Bi-Layer Interconnects using a Deformed Elastomeric Polymer Substrate," *Korean Journal of Metals and Materials,* vol. 51, pp. 151-158, Feb 2013.

[68] D. Y. Khang, H. Q. Jiang, Y. Huang, and J. A. Rogers, "A stretchable form of single-crystal silicon for high-performance electronics on rubber substrates," *Science,* vol. 311, pp. 208-212, Jan 13 2006.

[69] C. Yu and H. Jiang, "Forming wrinkled stiff films on polymeric substrates at room temperature for stretchable interconnects applications," *Thin Solid Films,* vol. 519, pp. 818-822, 2010.

[70] S. P. Lacour, J. Jones, S. Wagner, T. Li, and Z. G. Suo, "Stretchable interconnects for elastic electronic surfaces," *Proceedings of the Ieee,* vol. 93, pp. 1459-1467, Aug 2005.

[71] R. Huang, "Kinetic wrinkling of an elastic film on a viscoelastic substrate," *Journal of the Mechanics and Physics of Solids,* vol. 53, pp. 63-89, Jan 2005.

[72] C. M. Stafford, C. Harrison, K. L. Beers, A. Karim, E. J. Amis, M. R. Vanlandingham, *et al.,* "A buckling-based metrology for measuring the elastic moduli of polymeric thin films," *Nature Materials,* vol. 3, pp. 545-550, Aug 2004.

[73] C. Harrison, C. M. Stafford, W. H. Zhang, and A. Karim, "Sinusoidal phase grating created by a tunably buckled surface," *Applied Physics Letters,* vol. 85, pp. 4016-4018, Nov 1 2004.

[74] W. T. S. Huck, N. Bowden, P. Onck, T. Pardoen, J. W. Hutchinson, and G. M. Whitesides, "Ordering of spontaneously formed buckles on planar surfaces," *Langmuir,* vol. 16, pp. 3497-3501, Apr 4 2000.

[75] N. Bowden, S. Brittain, A. G. Evans, J. W. Hutchinson, and G. M. Whitesides, "Spontaneous formation of ordered structures in thin films of metals supported on an elastomeric polymer," *Nature,* vol. 393, pp. 146-149, May 14 1998.

[76] C. Yu, X. Li, T. Ma, J. Rong, R. Zhang, J. Shaffer, *et al.*, "Silicon Thin Films as Anodes for High‐Performance Lithium‐Ion Batteries with Effective Stress Relaxation," *Advanced Energy Materials,* vol. 2, pp. 68-73, 2012.

[77] K. Chen, E. Azhar, T. Ma, H. Jiang, and H. Yu, "Facile large-area photolithography of periodic sub-micron structures using a self-formed polymer mask," *Applied Physics Letters,* vol. 100, p. 233503, 2012.

[78] T. Ma, C. Lv, H. Liang, Z. Song, H. Huang, H. Wu, *et al.*, "Submicron pattern transfer in soft contact lithography using PDMS wrinkling masks," *Applied Physics Letters,* p. To be submitted, 2014.

[79] J. Aizenberg, J. Rogers, K. Paul, and G. Whitesides, "Imaging the irradiance distribution in the optical near field," *Applied physics letters,* vol. 71, pp. 3773-3775, 1997.

[80] J. A. Rogers, K. E. Paul, R. J. Jackman, and G. M. Whitesides, "Using an elastomeric phase mask for sub-100 nm photolithography in the optical near field," *Applied Physics Letters,* vol. 70, pp. 2658-2660, 1997.

[81] J. Aizenberg, J. A. Rogers, K. E. Paul, and G. M. Whitesides, "Imaging profiles of light intensity in the near field: applications to phase-shift photolithography," *Applied optics,* vol. 37, pp. 2145-2152, 1998.

[82] J. A. Rogers, K. E. Paul, R. J. Jackman, and G. M. Whitesides, "Generating~ 90 nanometer features using near-field contact-mode photolithography with an elastomeric phase mask," *Journal of Vacuum Science and Technology-Section B-Microelectronics Nanometer Structur,* vol. 16, pp. 59-68, 1998.

[83] T. W. Odom, J. C. Love, D. B. Wolfe, K. E. Paul, and G. M. Whitesides, "Improved pattern transfer in soft lithography using composite stamps," *Langmuir,* vol. 18, pp. 5314-5320, 2002.

[84] T. W. Lee, S. Jeon, J. Maria, J. Zaumseil, J. W. Hsu, and J. A. Rogers, "Soft‐Contact Optical Lithography Using Transparent Elastomeric Stamps and Application to Nanopatterned Organic Light‐Emitting Devices," *Advanced functional materials,* vol. 15, pp. 1435-1439, 2005.

[85] C. Vieu, F. Carcenac, A. Pepin, Y. Chen, M. Mejias, A. Lebib, *et al.*, "Electron beam lithography: resolution limits and applications," *Applied Surface Science,* vol. 164, pp. 111-117, 2000.

[86] B. J. Lin, "Deep UV lithography," *Journal of Vacuum Science and Technology,* vol. 12, pp. 1317-1320, 1975.

[87] L. A. Woldering, R. W. Tjerkstra, H. V. Jansen, I. D. Setija, and W. L. Vos, "Periodic arrays of deep nanopores made in silicon with reactive ion etching and deep UV lithography," *Nanotechnology,* vol. 19, p. 145304, 2008.

[88] K. Du, I. Wathuthanthri, W. Mao, W. Xu, and C.-H. Choi, "Large-area pattern transfer of metallic nanostructures on glass substrates via interference lithography," *Nanotechnology,* vol. 22, p. 285306, 2011.

[89] J. de Boor, N. Geyer, U. Gösele, and V. Schmidt, "Three-beam interference lithography: upgrading a Lloyd's interferometer for single-exposure hexagonal patterning," *Optics letters,* vol. 34, pp. 1783-1785, 2009.

[90] D. S. Kim, R. Ji, H. J. Fan, F. Bertram, R. Scholz, A. Dadgar, *et al.*, "Laser‐Interference Lithography Tailored for Highly Symmetrically Arranged ZnO Nanowire Arrays," *Small,* vol. 3, pp. 76-80, 2007.

[91] Y. Xia, J. A. Rogers, K. E. Paul, and G. M. Whitesides, "Unconventional methods for fabricating and patterning nanostructures," *Chemical Reviews,* vol. 99, pp. 1823-1848, 1999.

[92] L. J. Guo, "Nanoimprint lithography: methods and material requirements," *Advanced Materials,* vol. 19, pp. 495-513, 2007.

[93] H. Schift, "Nanoimprint lithography: an old story in modern times? A review," *Journal of Vacuum Science & Technology B,* vol. 26, pp. 458-480, 2008.

[94] J. Y. Cheng, C. Ross, E. Thomas, H. I. Smith, and G. Vancso, "Fabrication of nanostructures with long-range order using block copolymer lithography," *Applied physics letters,* vol. 81, pp. 3657-3659, 2002.

[95] M. K. Choi, J. Song, D.-K. Khang, H. Jiang, Y. Huang, and J. A. Rogers, "Biaxially Stretchable "Wavy" Silicon Nanomembranes," *Nano Letters,* vol. 7, pp. 1655-1663, 2007.

[96] R. Li, Y. Li, L. Chaofeng, J. Song, R. Saeidpouraza, B. Fang, *et al.*, "Thermo-mechanical modeling of laser-driven non-contact transfer printing: two-dimensional analysis," *Soft Matter,* 2012.

[97] D. Post, B. Han, and P. Ifju, *High sensitivity moiré: experimental analysis for mechanics and materials*: Springer, 1997.

[98] M. V. Kunnavakkam, F. M. Houlihan, M. Schlax, J. A. Liddle, P. Kolodner, O. Nalamasu, *et al.*, "Low-cost, low-loss microlens arrays fabricated by soft-lithography replication process," *Applied Physics Letters,* vol. 82, pp. 1152-1154, Feb 2003.

[99] C. S. Selvanayagam, J. H. Lau, X. Zhang, S. Seah, K. Vaidyanathan, and T. Chai, "Nonlinear thermal stress/strain analyses of copper filled TSV (through silicon via) and their flip-chip microbumps," *Advanced Packaging, IEEE Transactions on,* vol. 32, pp. 720-728, 2009.

[100] B. H. Jo, L. M. Van Lerberghe, K. M. Motsegood, and D. J. Beebe, "Three-dimensional micro-channel fabrication in polydimethylsiloxane (PDMS) elastomer," *Microelectromechanical Systems, Journal of,* vol. 9, pp. 76-81, 2000.

# APPENDIX A

# COPYRIGHT

This dissertation includes my published work. The detailed copyright permission is listed below.

Teng Ma*, Hanshuang Liang*, George Chen, Benny Poon, Hanqing Jiang, and Hongbin Yu. "Micro-strain sensing using wrinkled stiff thin films on soft substrates as tunable optical grating." Optics Express 21.10 (2013): 11994-12001. (*: Equal contribution). Copyright © 2013 The Optical Society.

Hanshuang Liang*, Teng Ma*, Hoa Nguyen, George Chen, Hao Wu, Hanqing Jiang, and Hongbin Yu. "High Sensitivity In-Plane Strain Measurement Using a Laser Scanning Technique." Electronic Components and Technology Conference (ECTC), 2014 IEEE 64rd. IEEE, 2014. (*: Equal contribution). Copyright © 2014 IEEE.

# APPENDIX B

## CO-AUTHOR APPROVAL

I verify that the following co-authors have approved the usage of our publication materials in the dissertation:

Hongbin Yu (Arizona State University)

Hanqing Jiang (Arizona State University)

Benny Poon (Intel Corp.)

Min Tao (Intel Corp.)

Teng Ma (Arizona State University)

George Chen (Arizona State University)

Hoa Nguyen (Arizona State University)

Cheng Lv (Arizona State University)

Rui Tang (Arizona State University)

Hao Wu (Arizona State University)